



HAL
open science

Eddy Surface Characteristics and Vertical Structure in the Gulf of Mexico from Satellite Observations and Model Simulations

Richard J. Brokaw, Bulusu Subrahmanyam, Corinne B. Trott, Alexis Chaigneau

► **To cite this version:**

Richard J. Brokaw, Bulusu Subrahmanyam, Corinne B. Trott, Alexis Chaigneau. Eddy Surface Characteristics and Vertical Structure in the Gulf of Mexico from Satellite Observations and Model Simulations. *Journal of Geophysical Research. Oceans*, 2020, 125, 10.1029/2019JC015538 . insu-03671101

HAL Id: insu-03671101

<https://insu.hal.science/insu-03671101>



Submitted on 18 May 2022

HAL is a multi-disciplinary open access archive for the deposit and dissemination of scientific research documents, whether they are published or not. The documents may come from teaching and research institutions in France or abroad, or from public or private research centers.

L'archive ouverte pluridisciplinaire **HAL**, est destinée au dépôt et à la diffusion de documents scientifiques de niveau recherche, publiés ou non, émanant des établissements d'enseignement et de recherche français ou étrangers, des laboratoires publics ou privés.

Copyright

Eddy Surface Characteristics and Vertical Structure in the Gulf of Mexico from Satellite Observations and Model Simulations

Richard J. Brokaw¹ , Bulusu Subrahmanyam¹ , Corinne B. Trott² ,
and Alexis Chaigneau^{3,4,5} 

¹School of the Earth, Ocean and Environment, University of South Carolina, Columbia, SC, USA, ²School of Ocean Science and Engineering, University of Southern Mississippi, Stennis Space Center, Hattiesburg, MS, USA, ³LEGOS, University of Toulouse, CNES, CNRS, IRD, UPS, Toulouse, France, ⁴Institut de Recherches Halieutiques et Océanologiques du Bénin (IRHOB), Cotonou, Republic of Bénin, ⁵International Chair in Mathematical Physics and Applications (ICMPA–UNESCO Chair), University of Abomey-Calavi, Cotonou, Republic of Bénin

Key Points:

- An eddy-tracking algorithm was applied in the Gulf of Mexico to examine biophysical characteristics
- Composites of anticyclonic and cyclonic eddies show surface and subsurface characteristics and vertical eddy structure
- Eddy properties vary between the eastern and western Gulf of Mexico due to air-sea interaction and differing long-term gradients

Correspondence to:

R. J. Brokaw,
rbrokaw@email.sc.edu

Citation:

Brokaw, R. J., Subrahmanyam, B., Trott, C. B., & Chaigneau, A. (2020). Eddy surface characteristics and vertical structure in the Gulf of Mexico from satellite observations and model simulations. *Journal of Geophysical Research: Oceans*, 125, e2019JC015538. <https://doi.org/10.1029/2019JC015538>

Received 31 JUL 2019

Accepted 5 FEB 2020

Accepted article online 11 FEB 2020

Abstract The Gulf of Mexico exhibits strong circulation due to the Loop Current System, along with high mesoscale eddy activity. In order to investigate eddy characteristics, we apply an automatic eddy-tracking algorithm to absolute dynamic topography maps and analyze the spatial distribution and evolution of eddy attributes including amplitude, radius, and eddy kinetic energy. The Loop Current region in the eastern Gulf of Mexico is an area of robust eddy generation for both cyclonic and anticyclonic eddies. Anticyclonic eddies were generally characterized by smaller amplitudes and larger radii when compared to their cyclonic counterparts. We also examine eddy surface properties including temperature and salinity anomalies as well as chlorophyll-a concentration and observe how these properties vary between the eastern and western Gulf of Mexico. Persistent features such as the Loop Current System and coastal low-salinity, highly biologically productive waters dominate eddy properties in the eastern side of the basin. We also apply the eddy-tracking algorithm to a regional Hybrid Coordinate Ocean Model validated using Argo floats. We find that this model accurately reflects surface characteristics in the mesoscale eddy field as well as the mean vertical eddy structure and use it to extend our analysis of eddy properties with depth. We find that subsurface characteristics of density, salinity, temperature, and velocities vary greatly between eddies in the eastern and western Gulf of Mexico. Through composite analysis of both surface and subsurface eddy properties, we gain a more complete picture of the mechanisms behind the observable characteristics of these eddies.

Plain Language Summary The Gulf of Mexico's surface circulation is dominated by the large-scale Loop Current System and mesoscale eddies. We apply an automatic eddy-tracking algorithm to absolute dynamic topography in the Gulf of Mexico. This algorithm aids in analyzing the spatial variability in eddy physical characteristics such as amplitude, radius, and eddy kinetic energy. We also observe the surface and subsurface properties of salinity, temperature, and chlorophyll-a concentration of these eddies and their surrounding waters. By separating the eddies based on circulation type (anticyclonic or cyclonic) and observing the depth structure of these eddies, we can better understand their dynamical characteristics. We also separate eddies based on their location in either the western or eastern Gulf. We find that the climatological features of the Loop Current and riverine discharge heavily affect eddy properties. This is seen in major differences in the temperature and salinity surface properties, as well as the vertical structure of eddies between the western and eastern Gulf of Mexico.

1. Introduction

Upper ocean circulation in the Gulf of Mexico (GoM) is dominated by the Loop Current (LC) and the associated mesoscale eddy field. The LC is a geostrophic current that flows northward through the Yucatan Channel and exits the GoM eastward through the Florida Straits (Sturges & Evans, 1983). The LC slowly grows within the GoM, stretching northward towards the Mississippi/Alabama/Florida (MAFLA) Shelf. This extended state leads to the regular shedding of large anticyclonic Loop Current eddies (LCEs), after which the LC returns abruptly to its retracted state (Alvera-Azcárate et al., 2008). LCEs have been observed to separate on time scales of approximately 3–17 months (Sturges & Leben, 2000). This separation is not a rapid event, nor is it easily measured, as meanders of the LC may detach and reattach several times before

completely separating and forming an LCE (Sturges et al., 1992). Once completely detached, this LCE drifts westward transporting relatively warm and salty water and eventually decays along the western GoM coast. This eddy separation has a seasonal peak in August and September, with a second, smaller peak in February and March (Hall & Leben, 2016). Additionally, smaller cyclonic eddies defined as Loop Current frontal eddies (LCFEs) congregate around the northern tip of an extended LC (Fratantoni et al., 1998; Paluszkiwicz et al., 1983; Vukovich, 1986). The growth of these LCFEs greatly affects the evolution of the LC at its neck near the Yucatan Strait as well (Walker et al., 2011). These LCFEs are suspected to play a key role in LCE detachment and formation (Cochrane, 1972) and have been documented to occasionally “pinch” the LC in its extended state, facilitating the shedding of LCEs (Zavala-Hidalgo et al., 2003). Formation of these LCFEs on both the eastern and western sides of the LC may be facilitated by vorticity perturbations from the Caribbean Sea (Sheinbaum et al., 2016). This prevalent mesoscale eddy field affects the redistribution of physical properties such as temperature and salinity, as well as biological characteristics such as chlorophyll-a (Chl-a) concentration (Brokaw et al., 2019; Morey, Martin, et al., 2003; Otis et al., 2019).

Mesoscale eddies typically exhibit different properties than their surrounding waters. They transport heat, salt, nutrients, and other biophysical characteristics throughout the oceans (Chaigneau et al., 2011; Chelton, Schlax, & Samelson, 2011; McGillicuddy et al., 2007). LCEs and other mesoscale eddies within the GoM can be distinguished by discernable differences of their properties in comparison to the GoM waters they flow through. Elliot (1982) demonstrated that the core of LCEs is comparatively warm and salty, with a steep salinity gradient along the eddy's radius. As the LCEs drift into the western GoM, they carry these seawater signatures with them, serving a role in the heat and salt budget of the entire Gulf (Elliot, 1982). These distinctly warm eddies can play a role in hurricane intensification within the GoM through latent and sensible heat flux (Gierach & Subrahmanyam, 2007). Historically, the temperature signature of the LC and LCE (measured using satellite infrared data) has been used to estimate LCE separation (Maul & Vukovich, 1993). However, this temperature-based method of inferring surface flow is hindered by consistently warm surface temperatures in the GoM during summer (Sturges & Leben, 2000). Now, satellite altimetry and multiparameter models are used to assess the surface circulation in the GoM (Alvera-Azcárate et al., 2008). This allows for more accurate estimation of eddy location, LCE shedding, and eddy characteristics.

The eddy characteristics exhibited at the surface can be due to air-sea interaction and vertical movements but may also be due to the eddy's interaction with the surrounding surface water through eddy trapping or eddy stirring (Dawson et al., 2018). Eddy trapping occurs during the formation of the eddy, during which the eddy may trap a water mass with anomalous characteristics at its center (Gaube et al., 2014). This trapped water mass is dynamically separated from the waters outside, preventing exchange outside of the eddy. Eddy stirring is the process by which the deformation of background gradients occurs due to the rotational velocity of the eddy (Chelton, Gaube, et al., 2011). Small, cyclonic LCFEs can entrain low-salinity water near the Mississippi Delta and transport this low-salinity water away from the northern GoM (Morey, Schroeder, et al., 2003). This entrainment is an example of eddy stirring by horizontal advection due to the cyclonic rotation of these LCFEs. Additionally, vertical eddy processes such as eddy pumping (Huang et al., 2017) and mixed layer modulation by eddies (Hausmann et al., 2017) can influence the biophysical properties at the surface.

The GoM's mesoscale eddy field is dominated by the large-radii, long living LCEs and because these LCEs carry great importance for both the biological productivity and hurricane intensification in this region, many previous studies of eddy characteristics have focused only on these LCEs. Leben and Born (1993) use sea surface height (SSH) fields from satellite altimetry to track eight LCEs over a 4-year period (April 1985–August 1989). Additionally, in situ observations from drifters and hydrographic surveys have been used to track and measure both surface and subsurface eddy characteristics in the GoM (Hamilton et al., 1999; Lewis et al., 1989; Rivas et al., 2008). However, these studies have likewise been focused exclusively on isolated LCEs. As part of the LC experiment that ranged from 2009 to 2011, much observational research was conducted that focused on the structure, variability, and underlying dynamics of the LC region (*Dynamics of Atmospheres and Oceans*: Issue 76, 2016). The associated papers (Donohue, Watts, Hamilton, Leben, & Kennelly, 2016; Hall & Leben, 2016; Hamilton et al., 2016; Lugo-Fernández et al., 2016; Rosburg et al., 2016; Sheinbaum et al., 2016) provide crucial information about the surface and subsurface dynamics of this region. In other regions of the world ocean, recent composite analysis of basin-wide mesoscale eddy fields has proved useful in identifying spatial patterns as well as differences in vertical structure and surface

characteristics between anticyclonic eddies (AEs) and cyclonic eddies (CEs). For example, Dawson et al. (2018) quantify biogeochemical cycling within eddies in the Southern Ocean, and Trott et al. (2019) make use of composite analysis to depict eddy-induced temperature and salinity changes in the Arabian Sea. First, this sort of basin-wide analysis of the mesoscale eddy field is lacking in the GoM. Additionally, studies such as Chaigneau et al. (2011) and Sun et al. (2018) depict composite vertical structures of eddies within the South Pacific and South China Sea, respectively, which help understand the differences between eddies of varying types in the vertical. Second, this type of vertical composite analysis is also absent for the GoM eddy field. The goal of this research is to first analyze eddy characteristics across the entire GoM without focus on one particular type of eddy. Once we complete this basin-wide analysis, we conduct composite analysis of surface eddy characteristics comparing AEs and CEs. We then investigate how these properties differ between the eastern and western sides of the basin. Finally, we conduct a composite analysis of the subsurface properties within these eddies, which help us understand the differences in the depth structure both between AEs and CEs and between the eastern and western GoM.

Satellite altimetry is extremely useful in expanding the knowledge of mesoscale eddy processes such as formation, detachment from the LC in the case of LCEs, and propagation because it provides estimates of SSH at high spatial and temporal scales. Investigation of eddy properties using multiple parameters from satellite observations helps improve our understanding of the spatial characteristics of both anticyclonic and cyclonic eddies in the GoM. We apply an automatic eddy-tracking algorithm to characterize GoM eddies and then quantify the spatial patterns of biophysical properties including salinity, temperature, and Chl-a concentration within these eddies. Satellite data are useful to describe eddy properties at the sea surface but do not allow us to investigate the vertical structure of the eddies and their impact on the water column with depth. In situ data, such as Argo floats or subsurface mooring arrays, provide very useful information about subsurface properties. Thus in this study, we use in situ data to validate a numerical model (Hybrid Coordinate Ocean Model [HYCOM]) with high temporal and spatial resolutions to observe the subsurface characteristics and vertical structure of these eddies. We first investigate the eddy surface properties in terms of eddy surface characteristics. We additionally justify the usage of this model comparing its ability to reproduce the vertical properties (temperature and salinity) observed from Argo floats. We then use this model to depict the vertical structure of the eddies, which provide insight to their subsurface properties. The primary objective of this study is to quantify the spatial patterns of eddy characteristics at the surface and with depth of eddies within the GoM using satellite-derived SSH (in this study, we have used absolute dynamic topography [ADT]), sea surface temperature (SST) and sea surface salinity (SSS), and HYCOM simulations. In section 2.1, we describe the satellite data and HYCOM simulations used in this study. Section 2.2 explains the eddy-tracking algorithm used to identify mesoscale eddies within the GoM. The results of surface and subsurface analyses of eddy properties are described in section 3. In section 4, we summarize the results and discuss the importance of the patterns we observe.

2. Data and Methods

2.1. Data

ADT, initially developed and processed by AVISO, is presently maintained by Copernicus Marine Environment Monitoring Service (CMEMS) and is available daily at a 0.25° horizontal resolution (www.copernicus.eu/en/services/marine). Compared to other oceanic satellite data, radar altimeters have long temporal coverage and do not experience contamination from cloud cover. We use the Global Ocean Gridded Level 4 SSHs data set provided by CMEMS, which merges research-quality observations from a variety of altimeter missions, including TOPEX/POSEIDON, HY2, Saral/AltiKa, Cryosat-2, Jason-1, Jason-2, Jason-3, ENVISAT, GFO, and ERS 1 and 2 and is homogenized to reference mission Jason-2 (Ducet et al., 2000; Le Traon et al., 1998). The full scope of this daily data set is from 1993 to present, but we use data from 2016–2018. Geostrophic currents plotted and used to compute eddy kinetic energy (EKE) in this study are derived from this data set.

SSS from NASA's Soil Moisture Active Passive (SMAP) mission is provided by NASA's Jet Propulsion Lab (SMAP SSS V4.2) at a 0.25° horizontal resolution (<https://podaac-tools.jpl.nasa.gov/drive/>; doi: 10.5067/SMP42-3TMCS). Daily data are derived using the 8-day running mean for complete spatial coverage over the full GoM. SMAP has been used extensively for GoM studies (Fournier et al., 2016; Vazquez-Cuervo

et al., 2018; Weissman et al., 2017). Vazquez-Cuervo et al. (2018) examined the performance of this satellite product in the GoM, finding good performance compared to in situ observations, particularly with respect to the seasonal cycle.

SST is from the National Oceanographic and Atmospheric Association National Climatic Data Center's Advanced Very High Resolution Radiometer optimally interpolated product available daily with a 0.25° resolution (Reynolds et al., 2007; www.ncdc.noaa.gov/oisst/data-access). This optimally interpolated product is preferred due to its lack of data gaps (both spatially and temporally) and has been used in eddy studies such as Dawson et al. (2018). We chose this product because the 0.25° spatial resolution is adequate for resolving mesoscale eddy features examined here and also matches the spatial resolution of the ADT and SSS data sets, removing a potential source of error by comparing product with different grid spacings. As for SMAP and ADT, the Advanced Very High Resolution Radiometer SST data set was extracted for the 2016–2018 period. Due to the advent of higher-resolution altimetry products (like that of the Surface Water and Ocean Topography mission to be launched in 2021), future work would do well to take advantage of higher-resolution SST satellites for identifying characteristics associated with the LC and eddies in the Gulf, particularly on the submesoscale level.

For satellite-derived ocean color, a 4-km resolution daily Chl-a product that merges Moderate Resolution Imaging Spectroradiometer and Visible Infrared Imaging Radiometer Suite sensor data was used from 2016–2018 (<http://hermes.acri.fr/>). Merging was done using the Garver–Siegel–Maritorena bio-optical model (Maritorena & Siegel, 2005), which is known for its consistency, ability to merge products regardless of their specific spectral bands, removes spectral band redundancies, and accounts for uncertainties from the normalized water-leaving radiance data streams.

To assess the entire vertical structure as well as mixed layer properties of eddies in the GoM, a regional $1/25^\circ$ HYCOM simulation was used that assimilates the Navy Coupled Ocean Data Assimilation system (Cummings, 2005). We use HYCOM GoM experiment 32.5 (available at hycom.org/data/goml0pt04/expt-32pt5), which provides sea level, geostrophic current, mixed layer depth (MLD), temperature, and salinity data. This regional HYCOM model has data available every hour from 1 April 2014. This model was subsampled every $1/4^\circ$ for appropriate comparison with the CMEMS product, converted to daily files by taking the daily average, and taken from 2016–2018 to remain consistent with satellite data. This regional model contains 40 total depth layers, but the top 22 vertical layers extending from the surface to 600-m depth are used. Although particularly intense eddies can extend deeper, these layers are sufficient to capture the mean vertical extent of the eddies as the density, temperature, and salinity cores as well as maximum swirl and vertical velocities are generally found above 600 m. A major advantage of HYCOM over other high-quality ocean models is its hybrid depth coordinate system, which are isopycnal in the open ocean, terrain following in shallow coastal regions, and z-level coordinates throughout the mixed layer (Bleck, 2002; Bleck & Boudra, 1981; Chassignet et al., 2003). Additionally, this regional HYCOM model assimilates altimetric and SST satellite data, as well as observational data from a variety of in situ sources including Argo floats, ship data, moorings, and buoys (Cummings, 2005). Due to the sufficient amount of altimeter data assimilated into HYCOM, there is no dependence on relaxation of climatological SSH, which increases our confidence in appropriately comparing eddying between the GoM HYCOM and the CMEMS products. Previous versions of GoM-specific HYCOM simulations (experiment 31.0) have been shown to have good agreement with observations and can provide information on larger spatial and temporal scales (Rosburg et al., 2016).

In order to validate the use of the regional GoM HYCOM model for observation of eddy characteristics with depth, we use data from a total of 3,550 Argo float profiles in the GoM during the 2016–2018 time period. These floats provide in situ temperature and salinity profiles reaching down to depths greater than 1,000 m. Here we use data for the top 600 m to capture the majority of eddy activity and in order to remain consistent with the HYCOM depths. The data used are part of the United States Global Ocean Data Assimilation Experiment courtesy of the Naval Research Laboratory in Monterey, CA and are available for public access (nrlgodae1.nrlmry.navy.mil/argo/argo.html).

2.2. Eddy Tracking

Using the technique initially proposed by Chaigneau et al. (2008) and Pegliasco et al. (2015) and recently used in Trott et al. (2018, 2019) or Aguediou et al. (2019), we apply an eddy-tracking algorithm to the

GoM. This method first defines each eddy center by identifying local ADT minima (CEs) and maxima (AEs) and then defines each eddy edge as the largest ADT closed contour surrounding the eddy center. An eddy edge must have at least four connected ADT points, resulting in a minimum radius of ~ 20 km in the GoM. Trajectories were created from individual eddies using the methodology described in Pegliasco et al. (2015). This eddy-tracking algorithm searches for eddy edge intersections between time t_1 and $t_1 + dt$ ($dt = 1$ day for the considered ADT product). If there are multiple intersections, we apply a cost function described in Trott et al. (2018) to determine the most statistically similar eddy. This method identifies eddies within one radius with the most statistically similar radius, amplitude, and EKE and selects it to continue the trajectory. Then the generation location is determined as the first eddy parts of each trajectory. During spatial analyses, pixels in which the total eddy count was less than 10 for the 2016–2018 period and therefore exhibited weak eddy density were not considered robust. These pixels were removed in order to depict accurate spatial maps of the mean eddy properties. Compared with other well-known eddy-tracking algorithms (Chelton, Gaube, et al., 2011; Souza et al., 2011; Yi et al., 2014), this technique identifies fewer false eddies and benefits from being threshold free.

Spatial anomalies of sea surface temperature (SSTA), sea surface salinity (SSSA), mixed layer depth (MLDA), and Chl-a concentration for surface properties as well as density, temperature, salinity, swirl velocity, and vertical velocity anomalies with depth were calculated by first averaging each parameter between the eddy center and one radius for each eddy. Then anomalies were computed in respect to the surrounding properties averaged between one radius and three radii from the eddy center.

Composite analysis was conducted for both surface and subsurface eddy properties. Each eddy was normalized by radius, and mean characteristics were plotted out to three radii. In these plots, north is plotted in the positive y -axis direction and east is plotted in the positive x -axis direction. Eddies were then separated by rotation type based on the local vorticity at the center of the eddy, as well as by location (eastern and western GoM). We choose to remove eddies in the Caribbean Sea to properly identify eddies in the eastern GoM by limiting the eastern GoM's latitudinal range to 21–32°N (Figure 1f).

3. Results and Discussion

3.1. Mean Large-Scale Characteristics

The long-term surface characteristics of sea level, temperature, salinity, Chl-a concentration, and MLD in the GoM respond very strongly to the inflow and circulation of the LC as well as river discharge, which are primarily observed in the eastern GoM. The climatological ADT and SSH show the mean position of the LC centered at 86°W and 25°N, the primary source of large AE generation in the form of LCEs. These LCEs propagate westward, and their ADT/SSH signature can be observed north of the Bay of Campeche in the western Gulf (Figures 1a and 1e). These eddies redistribute relatively warm and salty surface waters into the western GoM (Figures 1b–1g). The model shows a larger range of SSH values than altimeter-derived ADT, with higher values in the LC region and lower values along the northern coast of the GoM and the Bay of Campeche (Figure 1e). This difference between satellite and model output is not reflected in SST, but there is an interesting difference in satellite-derived and model SSS spatial gradients. Model SSS shows a much smoother gradient in extending southward to the central GoM and lower values of SSS in the western GoM than satellite-derived measurements. Coastal waters in the northern GoM generally have lower SST and SSS (Figures 1b and 1c) with average values of approximately 25 °C and 34 psu, respectively. This pattern is reflected in the model output as well (Figures 1f and 1g). These coastal regions also have the highest Chl-a concentrations (Figure 1d) surrounding the Mississippi River Delta and along the MAFLA Shelf of >1 mg/m³, mainly due to nutrient-rich riverine outflows from the Mississippi and Atchafalaya Rivers that provide nutrients necessary for high primary productivity. Conversely, offshore regions are found to have higher SST (~ 28 °C) and SSS (~ 36 psu), while also having lower Chl-a concentrations (~ 0.1 mg/m³). Model-derived MLD values near the coast do not exceed ~ 20 m, with greater values in the offshore western GoM (~ 35 m) and the largest in the eastern GoM near the LC region (~ 50 m; Figure 1h). The ADT/SSH, SST, and SSS values were compared for spatial correlation, and correlation coefficients (r) were found to be 0.98, 0.96, and 0.87, respectively. This spatial covariance indicates high spatial correlation between the satellite and model data sets, with the exception of SSS, which is most likely due to the difference in spatial extent of SSS gradient in the northern GoM (Figures 1c and 1g).

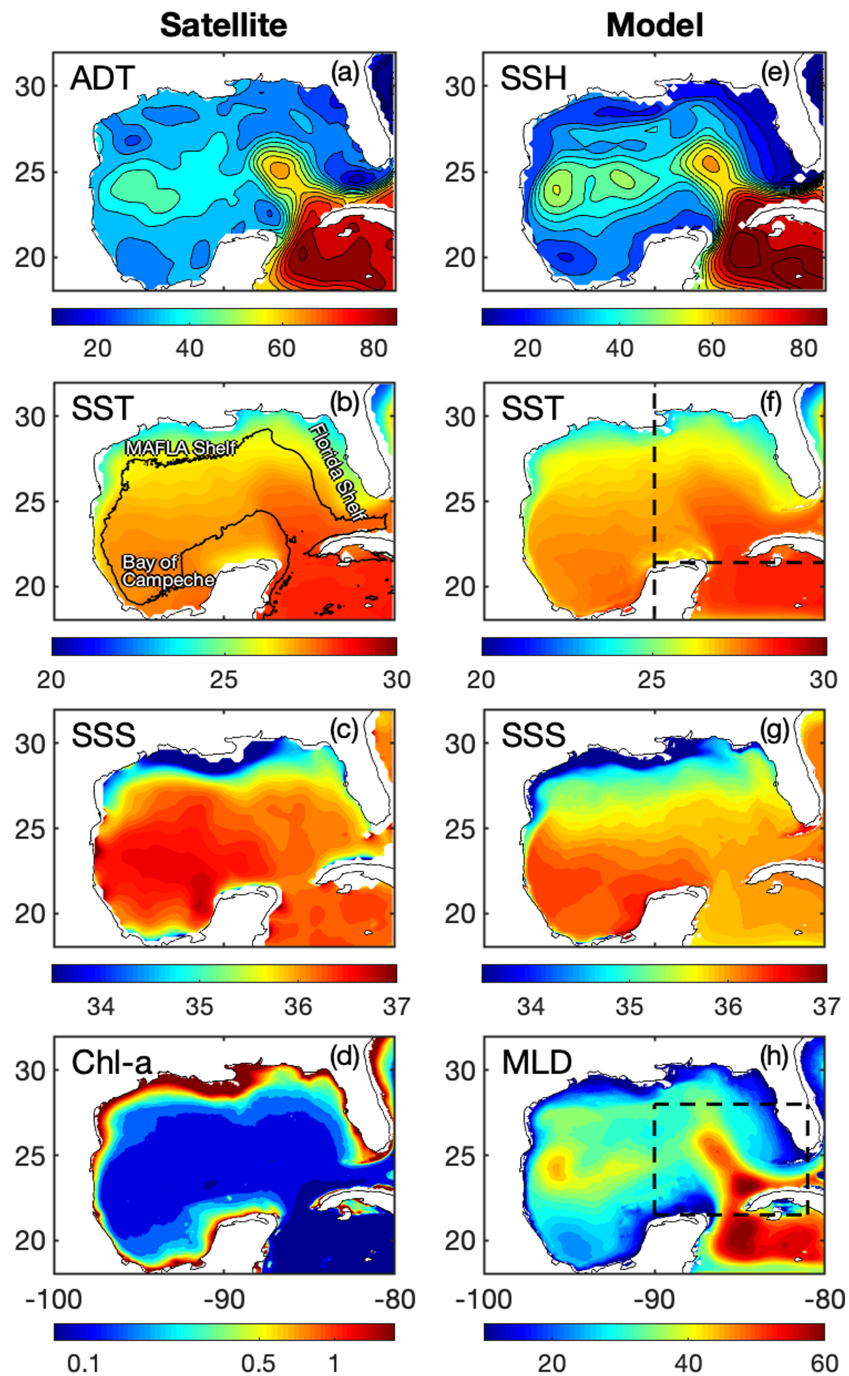


Figure 1. Climatological satellite-derived (a) absolute dynamic topography (ADT; centimeter); (b) sea surface temperature (SST; °C), the black line in (b) represents the 1,000-m isobath; (c) sea surface salinity (SSS; psu); (d) Chlorophyll-a concentration (Chl-a; mg/m^3); and model-derived (e) sea surface height (SSH; centimeter), (f) SST (°C), (g) SSS (psu), and (h) mixed layer depth (MLD; meter) for 2016–2018. Black dashed lines in (f) represent partitions used in composite analysis of western GoM, eastern GoM, and removing the Caribbean Sea. The black dashed box in (h) represents the area selected for box-averaged Loop Current eddy kinetic energy in Figure 3.

3.2. HYCOM Validation with Argo Profiles

In order to further validate the regional GoM HYCOM model for use in observing subsurface characteristics, we compare the HYCOM analysis with individual Argo float data. We compare the temperature and salinity data from a total of 3,550 Argo profiles in the GoM during the 2016–2018 period to match the temporal range

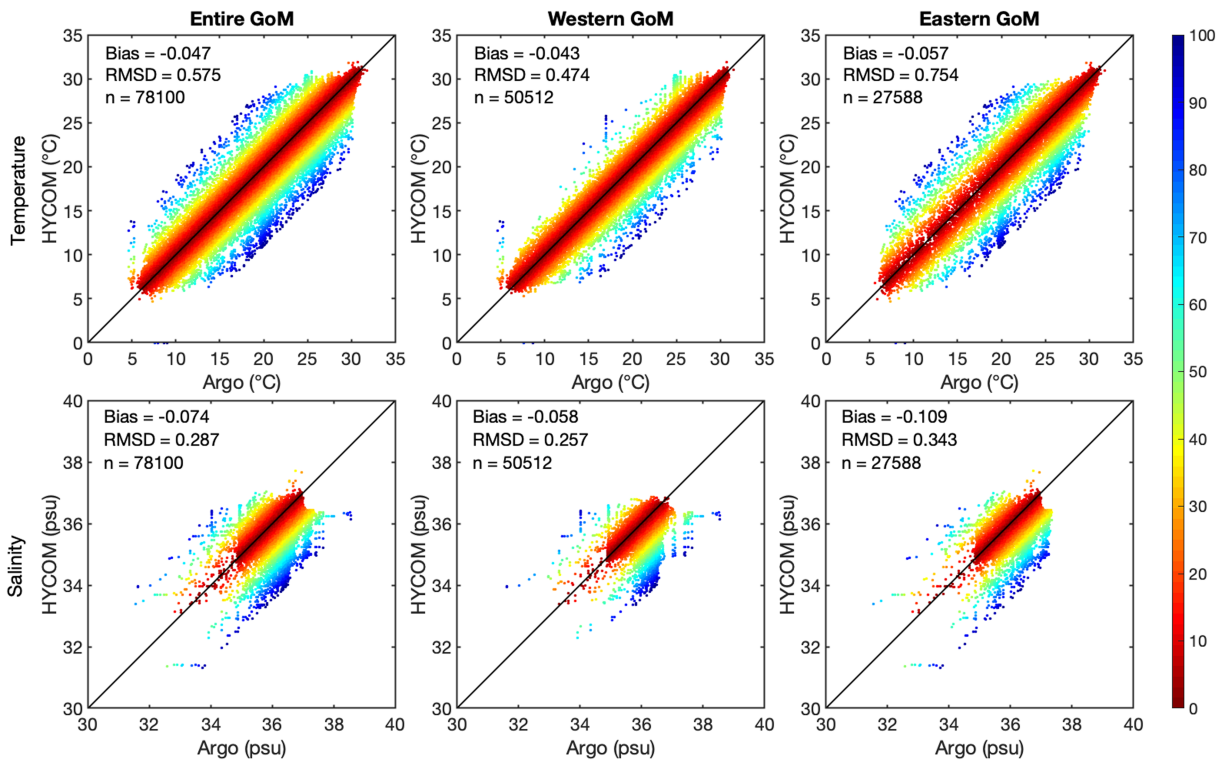


Figure 2. Scatterplots of HYCOM temperature (top; °C) and salinity (bottom; psu) versus Argo floats throughout the entire (left), western (center), and eastern GoM (right) from 2016–2018. Shading indicates percent variability, and the black line indicates a perfect 1:1 relationship.

of our study. First, the location of each Argo profile was matched to the nearest point at the surface in HYCOM. Then the Argo profiles were vertically subsampled at the 22 HYCOM depth levels (0–600 m). Figure 2 shows the scatterplot of collocated data with the mean bias (HYCOM–Argo) and root mean square (RMS) difference indicated in each plot.

We observe that overall, HYCOM tends to slightly underestimate both temperature (-0.05 °C) and salinity (-0.07 psu) observed in the Argo profiles, with RMS differences of 0.57 °C and 0.29 psu, respectively. We further compare the agreement between HYCOM and Argo across the western and eastern GoM. Of the 78,100 total Argo profile data points (3,550 profiles extracted on 22 levels) throughout the GoM during our study period, almost two thirds (50,512) were located in the western GoM, and approximately one third (27,588) were located in the eastern GoM. This could be due to overall tendency of the westward drift of the floats throughout the GoM as facilitated by LCE propagation and associated circulation (Pérez-Brunius et al., 2018). In terms of temperature, HYCOM performed better in the western GoM, with a lower RMS difference of 0.48 °C compared to the RMS difference of 0.75 °C found in the eastern GoM. A likewise pattern was found in salinity, with an RMS difference of 0.26 psu (0.34 psu) for the western (eastern) GoM. Additionally, a stronger mean fresh bias was observed in the eastern GoM (-0.11 psu) compared to the western GoM (-0.06 psu). These patterns could indicate that HYCOM does not capture temperature and salinity variability as well in the eastern GoM than the western GoM. However, statistical significance tests (two-way t tests) suggest that the differences between the HYCOM and Argo values both basin-wide and within each subbasin are not significant beyond the 95% significance level. Therefore, we are confident in that HYCOM correctly reproduces the large-scale distribution of temperature and salinity properties and their variability throughout the GoM.

3.3. Temporal Evolution of Eddy Characteristics

The evolution of eddy characteristics of all eddies identified in both satellite and model data with time, as well as the distribution of these characteristics is shown in Figure 3. The number of daily identified eddies of each circulation type in the GoM did not exceed 20, with maximum daily values of 19 AEs (18 January

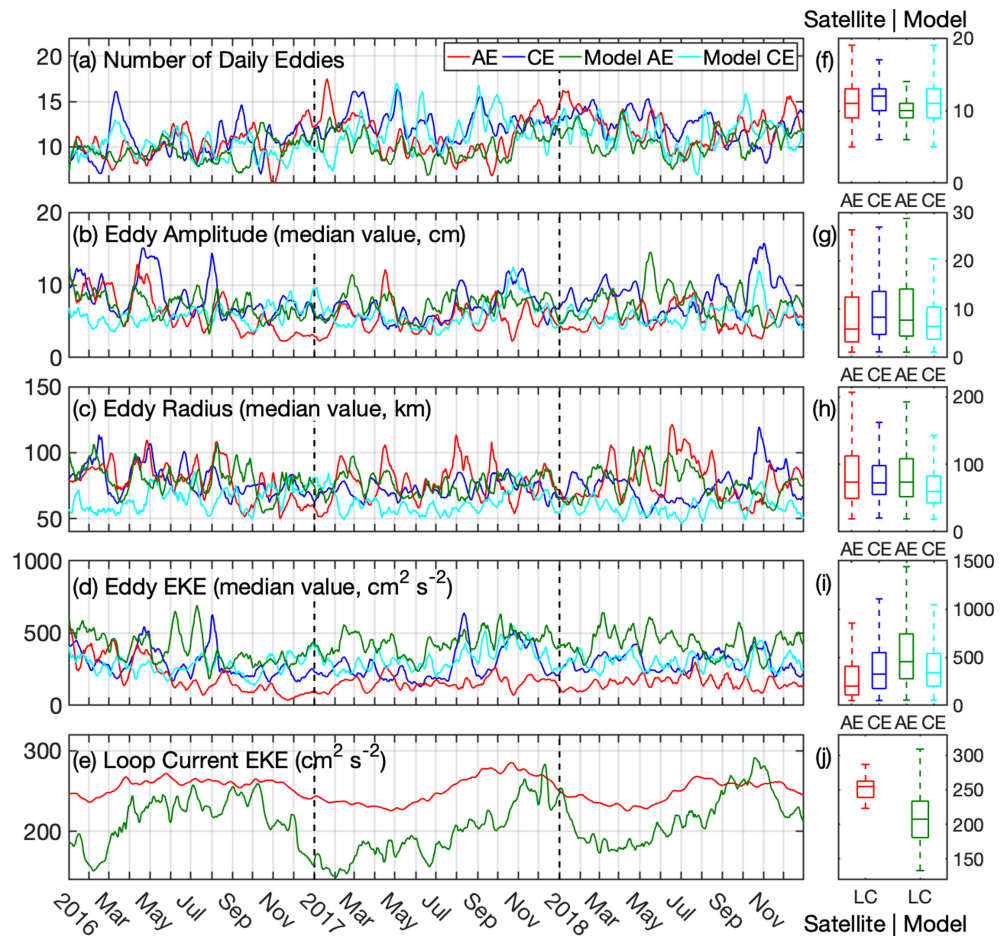


Figure 3. Evolution of eddy characteristics (a–e) from 2016–2018 for satellite and model data showing anticyclonic (red and green) and cyclonic (blue and cyan) eddies and boxplots (f–j) showing the mean, upper and lower quartiles, and minimum and maximum of these characteristics. Characteristics: (a, f) number of eddies, (b, g) eddy amplitude, (c, h) eddy radius, (d, i) eddy EKE, and (e, j) Loop Current EKE.

2017; satellite) and 17 CEs (2 May 2017; model; Figure 3a). Generally, periods displaying high numbers of CEs were accompanied by low numbers of AEs and vice versa (seen in March 2016, January 2017, and May 2017). During these periods, the ratios of CEs to AEs were 16:3, 11:18, and 16:8, respectively. However, there were notable periods displaying high numbers of daily eddies of both types (e.g., January 2018), at which point, the values of eddy amplitude (radius) were below average with values of ~ 7 cm compared to mean ~ 8 cm (~ 60 km compared to mean ~ 75 km).

Eddy amplitudes remained relatively consistent (typically 7 to 8 cm), except for a few high-amplitude CE events in May and August 2016 and November 2018 where median eddy amplitudes reached upwards of 17 cm (Figure 3b). These high-amplitude events are reflected in the radii (Figure 3c) and EKEs (Figure 3d). The distributions of AEs and CEs between satellite and model data are similar in number of daily eddies (Figure 3f) and eddy radius (Figure 3h), with both satellite and model output indicating more daily CEs and larger radius AEs. CEs were much more energetic than AEs throughout the time series and on average in the satellite data, but model output showed higher EKE for AEs (Figures 3d and 3i). Satellite anticyclonic (cyclonic) EKE displayed a mean value of $132 \text{ cm}^2 \text{ s}^{-2}$ ($287 \text{ cm}^2 \text{ s}^{-2}$) whereas the model showed mean anticyclonic (cyclonic) EKE values of $493 \text{ cm}^2 \text{ s}^{-2}$ ($290 \text{ cm}^2 \text{ s}^{-2}$). This result that points to more energetic CEs in the GoM is contrary to the idea that AEs that are larger in size and penetrate deeper than CEs should be more energetic. However, this difference may be due to data assimilation. Satellite and model output show opposite patterns in eddy amplitude and EKE (Figures 3g and 3i), in which the satellite shows higher CE amplitude and EKE, but the model displays higher AE amplitude and EKE. This could be

due to the assimilation of Argo data into HYCOM. Luecke et al. (2017) compare global mesoscale energy between HYCOM and Argo and find similarities in EKE. Since both the HYCOM model and the merged altimetry product use raw altimeter data, it is likely that the assimilation of Argo data in HYCOM is causing this difference. HYCOM may therefore display a more comprehensive view of EKE in the LC region due to the assimilation of both surface and subsurface data. Another possible explanation for this difference could be that the HYCOM EKE includes both geostrophic and ageostrophic motions, while the EKE computed from satellite altimetry is solely based on geostrophic velocities. While the median eddy EKE time series reflects the state of the entire GoM mesoscale eddy field, Figure 3e reflects the state of the LC region.

Following the methodology used in Donohue, Watts, Hamilton, Leben, Kennelly, and Lugo-Fernández (2016), we box averaged the EKE in the eastern GoM from 90–81°W and 21.5–28°N (shown in Figure 1h) and plotted the EKE for AEs found within this box. Our box is bigger than that used by Donohue et al. because we are not limited to the coverage of mooring data and are able to fully cover the LC and its eddies at the surface. When LC EKE is high, the LC is typically extended or has recently shed a large LCE. In 2016, the LC remained extended from March–December, while in 2017, the LC was only extended from September–December. In 2018, the maximum LC EKE was the lowest of the three years. Similar to EKE (Figures 3d and 3i) and the ADT/SSH presented in Figures 1a and 1e, the model shows a larger range of LC EKE values, ranging from 133–306 cm^2/s^2 , while the LC EKE calculated from satellite data was higher on average with a narrower range from 223–287 cm^2/s^2 . These EKE values are lower than those found in Donohue et al. Since our measures are at the surface, and those of Donohue et al. are at 200 m, one would expect our values to be higher. However, this difference in values is most likely due to the fact that our measure uses a box-averaged EKE over the larger LC region, which will therefore include eddies of smaller EKE within the area, whereas in Donohue et al., moorings are used. Although our values of EKE are comparatively small, they nonetheless show the increase observed during the growing of the LC and subsequent decrease when a large LCE is shed. An analysis of variance test conducted on the boxplot data indicates that the mean values of all parameters when compared between the satellite data and model simulations are not statistically different at the 95% significance level.

3.4. Spatial Variation of Eddy Characteristics

Eddy characteristics throughout the GoM vary greatly between AEs and CEs, responding to the intrusion of the LC, the shape of the basin, and the overall local anticyclonic circulation. The mean spatial distribution of AEs and CEs (Figures 4a–4d) is highly varied, though some spatial patterns are apparent. The Caribbean Sea exhibits a high number of AEs most likely due to the overall anticyclonic rotation near the source of the LC in the Caribbean Sea. Additionally, the decay of LCEs that have propagated westward helps establish anticyclonic rotation in the southwestern GoM (Chang & Oey, 2010). This propagation of LCEs meets the overall cyclonic circulation in the Bay of Campeche as well as the western boundary, which then helps facilitate the dissipation of these eddies (Pérez-Brunius et al., 2018). Conversely, the central Gulf contains much more CEs, which is reflective of the distribution of LCFEs that surround the LC in this region (Fratantoni et al., 1998). AEs generally possess larger radii (100–150 km) throughout the GoM between 22° and 27°N (Figures 4e and 4g), though CEs present across the entire GoM and Bay of Campeche exhibit much smaller radii (70–100 km). The same was found to be true for eddy amplitudes (Figures 4i–4l) with maximum AE (CE) amplitudes ranging from 20 to 30 km (10–20 km), although CEs were shown to have larger amplitudes than AEs on average through the time series (Figure 3b). The largest amplitude CEs are found in the LC region (19–22 cm) and decrease in amplitude along the path of LCE propagation. This is most likely a signature caused by smaller CEs that are found to congregate around the circulation of the LC (Figures 4j and 4l), as well as previously shed LCEs (Walker et al., 2009). These CEs likely include the LCFEs that play a role in LCE detachment (Zavala-Hidalgo et al., 2003). CEs tend to decay over the deep central GoM water at the tip of an extended LC (Hamilton et al., 2016). The presence of these LCFEs at the base of the LC near the Caribbean Sea is also most likely the reason for the observed high cyclonic EKEs in this region (Figures 4n and 4p). EKEs are consistently higher in AEs than CEs (Figures 4m–4p) in the extended LC region, whereas the highest EKE in CEs is found near the base of the LC. High EKEs in the extended LC region are most likely due to LCE shedding, during which enhanced EKE peaks (Donohue, Watts, Hamilton, Leben, & Kennelly, 2016). The model shows more extreme values of EKE in AEs ($>1,400 \text{ cm}^2 \text{ s}^{-2}$) than the satellite ($\sim 1,000 \text{ cm}^2 \text{ s}^{-2}$), which is reflective of the pattern shown in Figure 3i. The extremely low mean ADT/SSH just north of the Yucatan

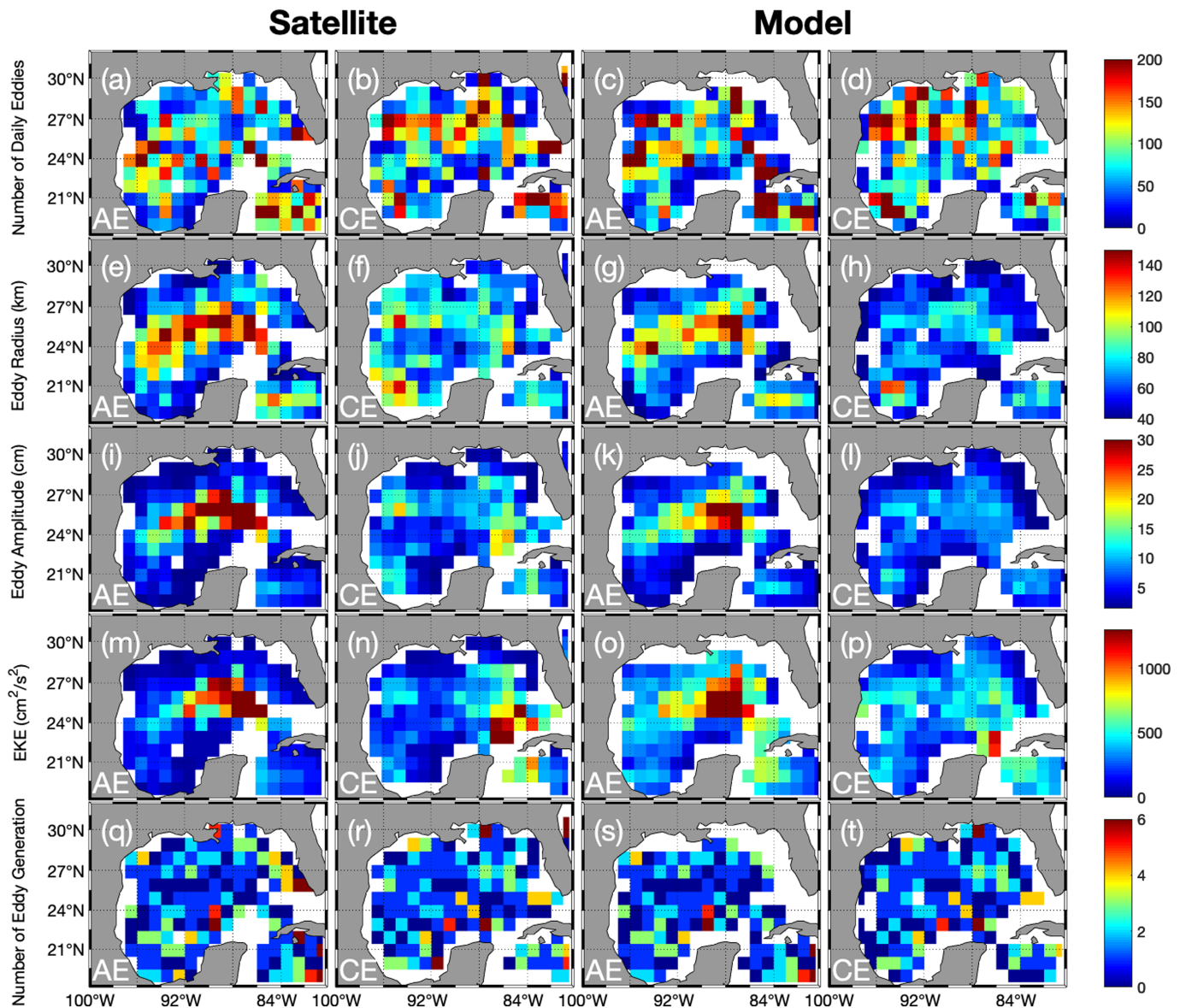


Figure 4. Mean spatial distribution of eddy characteristics during 2016–2018 between satellite (left) and model (right) for anticyclonic (first and third columns) and cyclonic (second and fourth columns) eddies. (a–d) Number of eddies, (e–h) eddy radius (kilometer), (i–l) eddy amplitude (centimeter), (m–p) EKE (cm^2/s^2), and (q–t) number of eddy generation. Pixels with less than 10 eddies were discarded.

Peninsula shown in Figures 1a and 1e, which is likely an artifact of cyclonic LCFEs in this area, helps explain the abundance of high-energy CEs located in this region. Eddy generation locations are extremely spatially variable but show consistently low coastal generation. The fact that the generation locations are almost identical between satellite and model data suggest that the differences between the two methods observed in other characteristics occur during the eddy's lifetime. The overall distributions of characteristics are very similar; however, the model underestimates the magnitude of all AE/CE characteristics (radius, amplitude, and EKE) along the coast and overestimates EKE in the open central GoM waters.

Eddies of both circulation types were observed everywhere within the GoM except some coastal regions such as the northeastern GoM (96°W and 28°N), the west Florida Shelf (84°W and 27°N), and the eastern Bay of Campeche (approximately 92°W and 21°N). A high number of CEs were found in the western Bay of Campeche (~ 175 ; Figures 4b and 4d), which is consistent with the subbasin's overall cyclonic circulation. EKE values that are relatively high for CEs ($\sim 500 \text{ cm}^2/\text{s}^2$) were also found in this region, which is likely

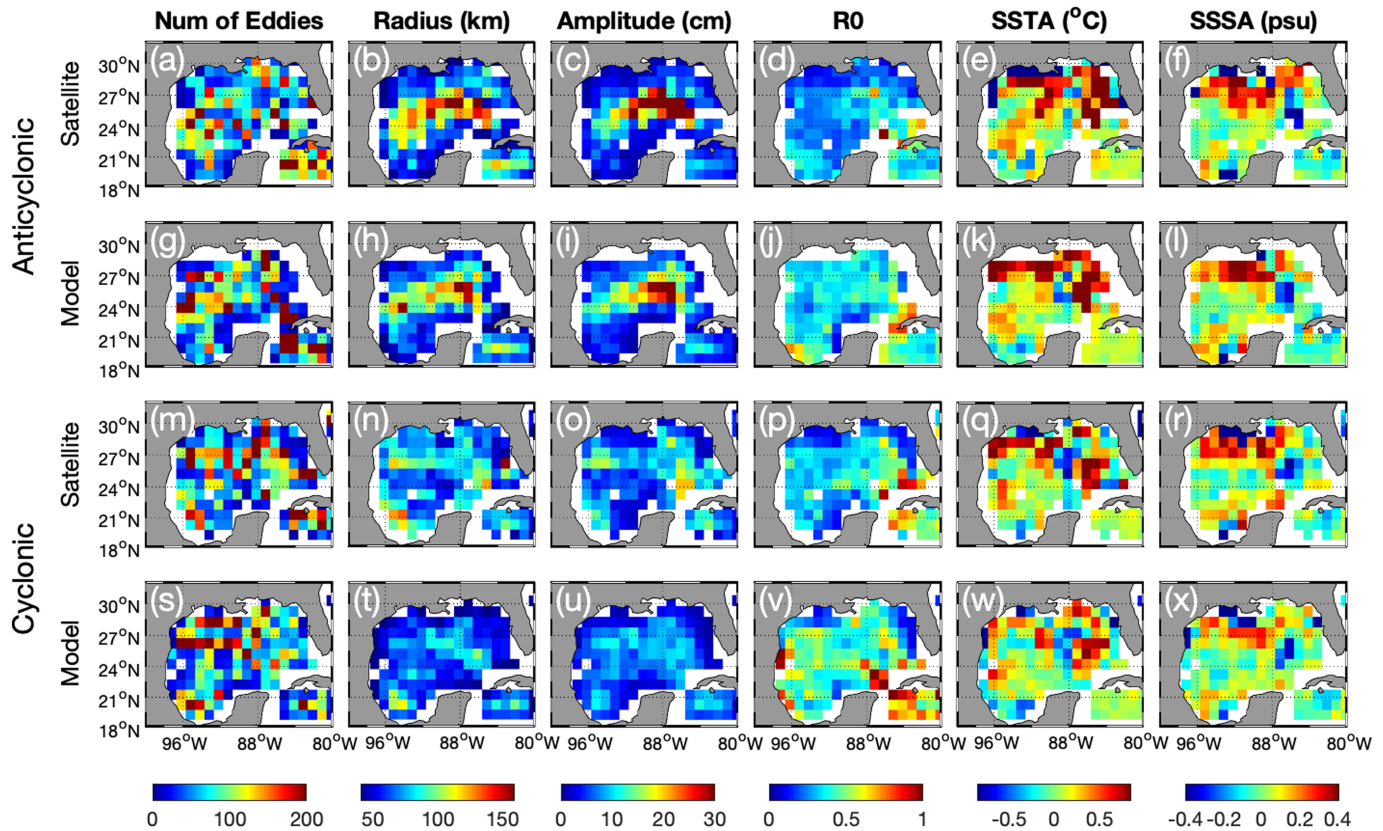


Figure 5. Mean spatial distribution of eddy characteristics from 2016–2018. Characteristics are (left to right) number of eddies, radius (kilometer), amplitude (centimeter), Rossby number, SSTA (°C), and SSSA (psu) separated by anticyclonic and cyclonic eddies for both satellite and model data. Pixels with less than 10 eddies were discarded.

due to the westward intensification in this area (Vazquez de la Cerda et al., 2005). The cyclonic eddy generation northwest of Campeche bank was observed by Zavala-Hidalgo et al. (2003) and is attributed to LC dynamics due to the eddy generation timings. This region in the western GoM was a region of large-radius CEs (Figures 5n and 5t). Similar to the physical characteristics shown in Figure 4, the spatial distributions between satellite-derived (Figures 5a–5f and 5m–5r) and model-derived (Figures 5g–5l and 5s–5x) eddy properties show similar regional patterns (e.g., high SSTA in the LC region). However, the magnitude of these properties varies between the satellite and model. While both the satellite and model identify large-radius and large-amplitude AEs in the LC region and along the path of LCE propagation, the model underestimates the magnitude of these qualities. Satellite data show radii in this region of approximately 110–160 km, while model output indicates radii of approximately 90–150 km. In amplitude, the satellite and model both show values greater than 30 cm in the LC region, but the model amplitudes are not as large (15–20 cm compared to 25–30 cm in satellite) toward the western part of the basin. Additionally, the magnitude of radius and amplitude for CEs is lower in the model across the entire GoM, with some areas of especially notable underestimation. The first is the western Bay of Campeche (approximately 96–94°W and 21°N) in which satellite (model) data estimate values of radius and amplitude to be 130 km (110 km) and 15 cm (10 cm), respectively. Another area is near the base of the LC region (approximately 88–86°W and 23°N) where satellite (model) data show radius and amplitude to be 70 km (50 km) and 20 cm (8 cm), respectively.

Higher values of Rossby number ($R_0 = 0.8$ – 1) were found in the LC region across both AEs and CEs when compared to the rest of the GoM, indicating that inertial and centrifugal forces dominate in this region and flow is most likely ageostrophic. The difference in magnitude of R_0 between satellite data and model output is unlike that of radius and amplitude. HYCOM tends to overestimate R_0 in both AEs and CEs, especially in the LC region. This is most likely due to the nonlinear HYCOM field that is strongly affected by large-scale

nonlinear flows like Ekman transport (Douglass & Richman, 2015). Douglass and Richman (2015) also show this tendency of HYCOM to overestimate R_0 . By comparing HYCOM-derived R_0 to R_0 calculations based on geostrophic velocity fields computed from SSH, they show that HYCOM estimates of R_0 are approximately 0.5 higher than those from SSH in the tropical Atlantic.

The spatial distribution of SSTA was somewhat patchy although some climatological features as seen in high SSTA can be observed. There is a patch of high SSTA values centered at approximately 86°W from 26–27°N in both satellite and model maps of AEs (Figures 5e and 5k). This patch is centered around the mean position of an extended LC (Figures 1b and 1f), where relatively warm water from the Caribbean Sea flows northward into the GoM. On the other hand, areas of low SSTA at the eddy center can be found in the northern GoM coastal regions. This may be due to the seasonal river discharge, which can deposit colder waters from early spring snow melt over the northern part of the Mississippi River watershed into the coastal GoM (Bratkovich et al., 1994). AEs are expected to have positive SSTAs at their center; however, this patch of high SSTA is also partially visible in satellite and model maps of CEs (Figures 5q and 5w), which suggests that this signal is representative of the high SST observed in the LC region through climatology (Figures 1b and 1f). Another feature is the anomalously cold SSTAs found at approximately 88°W and 26°N in both AEs and CEs (Figures 5e, 5k, 5q, and 5w). This is most likely due to the location of these eddies surrounding the LC. Since the LC is observed to have very high SSTs in this region due to the inflow of Caribbean Sea waters, it is likely to have affected the calculations of AE and CE SSTAs in the surrounding waters, as anomalies were computed out to three eddy radii.

The spatial distribution of SSSA throughout the GoM was similar across eddies of both circulation types in both the satellite and model data. Both AEs and CEs were observed to have negative SSSAs (0.3–0.4 psu) in the southeastern GoM (centered at 86°W and 25°N), suggesting that both types of eddies can redistribute relatively fresh water from Mississippi River outflow to the LC region. Interestingly, this area exhibits high SSTA values in both AEs and CEs (higher than 0.75 °C), so this negative SSSA signature is likely not a result of eddy-induced upwelling, as would only be seen with CEs, or other vertical processes associated with the mesoscale eddy field. Although AEs and CEs have different physical characteristics (radius and amplitude), surprisingly there is little difference in their impact on SST and SSS. We can therefore assume that the surface properties of SSTA and SSSA within each eddy are more likely driven by air-sea interaction or horizontal advection of the background large-scale field and persistent features (those shown in Figure 1) rather than vertical movements associated with the mesoscale eddy field.

3.5. Isolated Eddies

In order to observe eddy characteristics such as salinity and temperature through depth, we have isolated one CE centered at (93°W and 26°N) on 1 August 2017 using satellite-derived measures of ADT, SSS, SST, and Chl-a concentration (Figures 6a–6d). We choose to isolate this eddy since it is a relatively large CE whose size can aid in the observation of finite mechanisms such as eddy stirring (Chelton, Gaube, et al., 2011) that lead to high Chl-a concentrations and low salinity values within the eddy. We then observe the characteristics of density, salinity, temperature, and vertical velocity with depth using model output (Figures 6e–6h). The SSS signature of this eddy shows anomalously fresh water (~33.5 psu) at the core (Figure 6b). Given the location of this eddy at 93°W and 26°N near the MAFLA Shelf, this low-salinity signature is most likely a result of the trapping of coastal waters that are sourced from Mississippi and Atchafalaya Rivers discharge. The high Chl-a concentration (~0.25 mg/m³; Figure 6d) at the core of this eddy also supports this mechanism. McGillicuddy (2016) describes a situation in which there is a strong northward Chl-a gradient and where a counterclockwise-rotating (CE in this case) eddy would advect this high Chl-a water along its northwestern edge. This advection and eddy stirring is visible in this isolated eddy, which leads to a positive Chl-a anomaly at its center compared to the outside concentration. This eddy is representative of the spatial salinity and radius patterns shown in Figure 5. Its anomalously low-salinity core helps contribute to the tendency of negative SSSAs to be located near the coast in the northwestern GoM (Figures 5r and 5x). This eddy is anomalously large, however, with a radius of 169 km, which is not representative of the spatial tendency in the northwestern GoM towards relatively low-radius CEs. The mean radii of CEs in the northwestern GoM is approximately 75 km (Figures 5n and 5t).

The upwelling of subsurface water is shown in the strong vertical velocities reaching 2.5 mm/s from approximately 100- to 600-m depth near the center of the eddy (Figure 6h). This upwelling injects high-salinity water

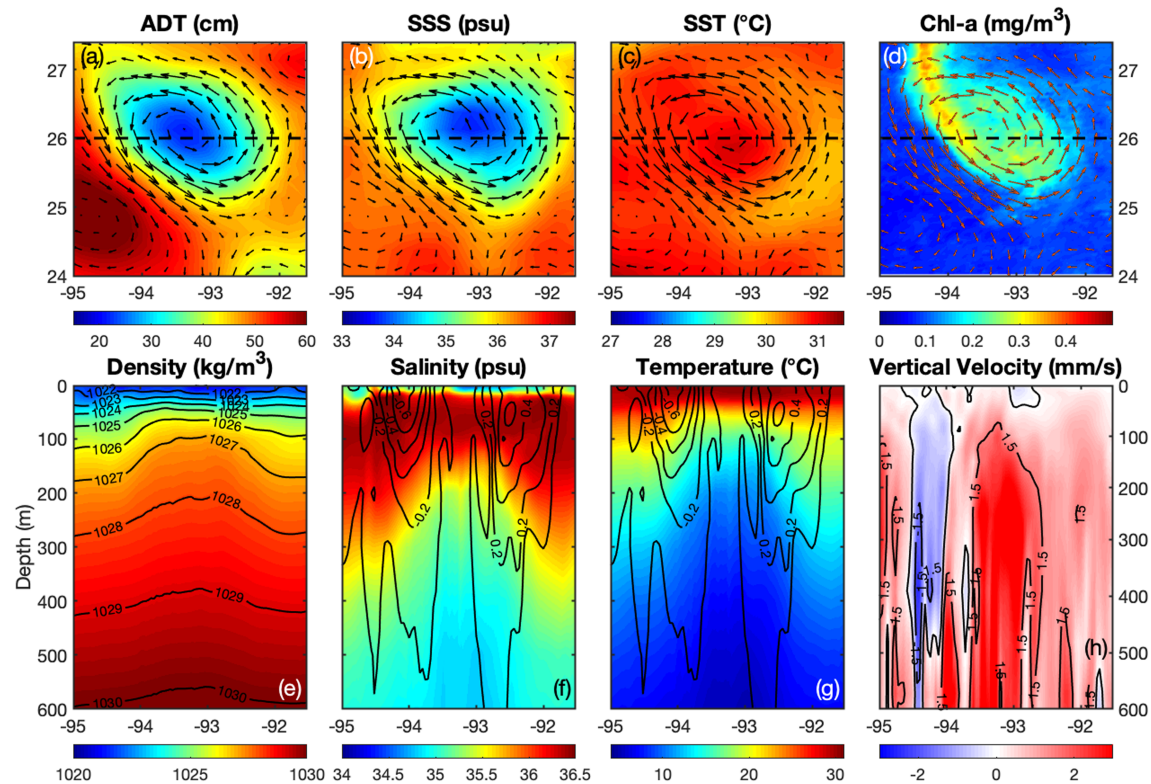


Figure 6. Eddy characteristics of a CE centered at approximately 93°W and 26°N on 1 August 2017. (a) ADT (centimeter), (b) SSS (psu), (c) SST (°C), and (d) Chl-a concentration (milligram per cubic meter) and geostrophic current vectors from satellite observations. HYCOM (e) density (kilogram per cubic meter), (f) salinity (psu), (g) temperature (°C), and vertical velocity (millimeter per second); contoured every 1.5 mm/s zonal cross sections at the dashed line indicated in (a–d). Black contours in (e) indicate isopycnals every 1 kg/m³. Black contours in (f and g) indicate swirl velocities (meridional component; meter per second) every 0.1 m/s.

(~36–36.5 psu) into the surface layers (Figure 6f), which erodes the surface salinity minimum. This upwelling signature is also seen in low-temperature (<12 °C) water moving towards the surface near the center of the eddy (Figure 6g). The swirl velocity within the eddy shows speeds of 0.2 m/s extending from the surface down to 300-m depth, with velocities of 0.1 m/s reaching below 600 m. The maximum swirl velocity of ~0.5 m/s is observed below the surface at approximately 50- to 80-m depth into the pycnocline (Figures 6f and 6g). This observation, along with the vertical density structure, helps identify this eddy as likely subsurface intensified due to the deepening of surface isopycnals down to ~20 m but doming of subsurface isopycnals up to ~90 m (Figure 6e).

The isolated AE shown in Figure 7 is likewise located in the northern central GoM centered at 91°W and 26°N). This eddy, like the CE shown in Figure 6, is anomalously large, with a radius of 203 km compared to the average of 80 km (Figure 3h). Given its size and the fact that this eddy was generated in the LC region helps us characterize it as a distinctive previously shed LCE. We choose a large eddy in order to observe mesoscale processes specific to each eddy such as the horizontal advection of low-salinity waters and waters with high Chl-a concentration sourced from riverine input. This isolated eddy represents an ideal interaction of an AE with a northward gradient of freshwater and Chl-a similar to McGillicuddy (2016) and may not be representative of all AEs found in the GoM. However, examination of these processes is conducted prior to future composite analysis (section 3.6) in order to investigate whether the processes observed in this isolated instance have an observable effect on mean eddy properties. Low-salinity water (~34–34.5 psu) can be observed along the eastern and southern edges of this LCE (Figure 7b), with Chl-a concentration displaying a similar pattern (Figure 7d). As its position indicates that this eddy is located just south of the MAFLA Shelf, we can conclude that this AE advects the low-salinity, high-nutrient water off of the shelf and over the deep central GoM. These surface characteristics are indeed representative of the spatial patterns of AEs in this area shown in Figure 5. This isolated eddy confirms the tendency for large-radius AEs to be found in the central GoM along the path of LCE propagation.

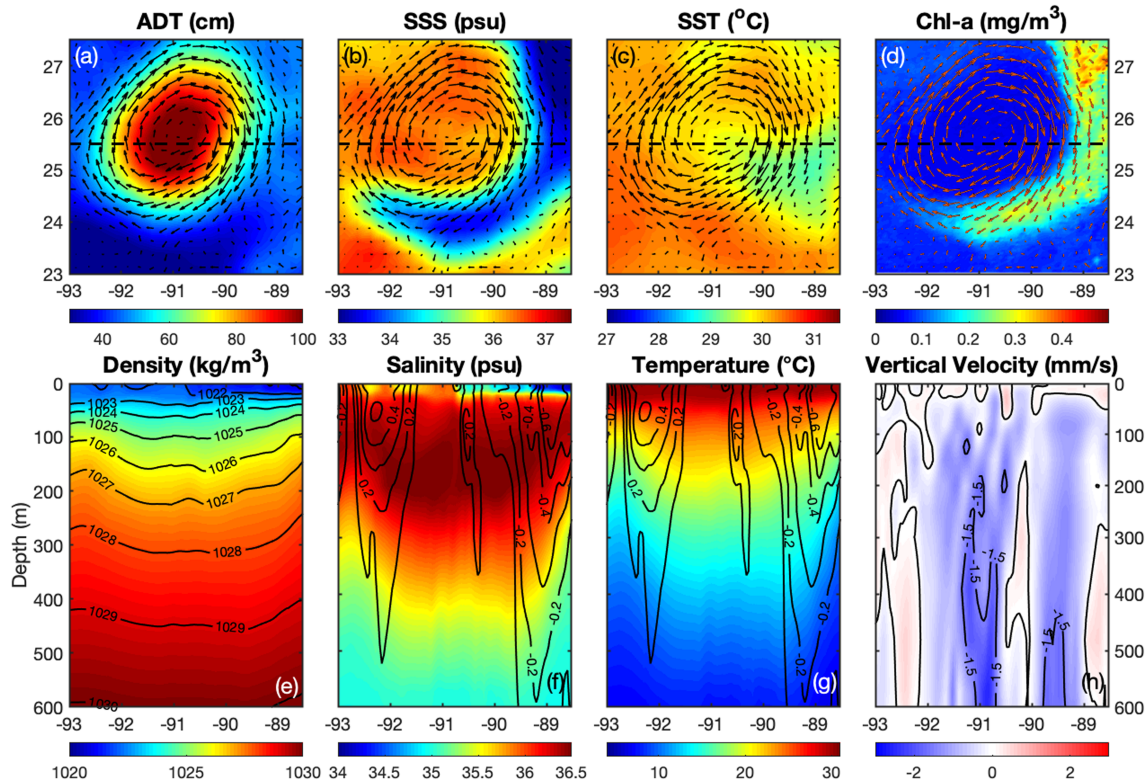


Figure 7. Same as Figure 6 but of an AE centered at approximately 91°W and 26°N on 30 August 2016.

With depth, it is clear that the low-salinity water along this eddy's eastern edge only penetrates to approximately 30-m depth. Further investigation into the subsurface properties of density, salinity, temperature, and vertical velocity within this eddy reveals downwelling. This is evident first in the deepening of isopycnals down to ~450 m (Figure 6e). Additionally, the subsurface salinity maximum (>36.5 psu) occurs at approximately 100–250 m, but this high-salinity water also extends down past 400-m depth within the eddy (Figure 7f). Likewise, the vertical extent of high-temperature waters (>20 °C) reaches down to 300-m depth (Figure 7g). The negative vertical velocities (approximately –1.8 mm/s) reaching from approximately 50- to 600-m depth (Figure 7h) indicate that downwelling is the mechanism by which the subsurface salinity maximum and warm-temperature waters extend downward and contributes to the deepening of the isopycnals seen in Figure 7e. The vertical velocities observed in this eddy are similar to those typical of LCEs wherein Rivas et al. (2008) observe downward vertical velocities of 2 and 3 mm/s using in situ data from moorings and acoustic Doppler current profilers. Similar to the CE shown in Figure 6, the maximum swirl velocity of ~0.6 m/s is found below the surface from 30- to 100-m depth.

3.6. Composite Analysis of Eddy Surface Properties

Composite analysis of AEs (Figure 8) and CEs (Figure 9) throughout the GoM reveals how eddies of each type vary at the surface. Here we separate eddies not only based on rotation type but also based on their location within the western or eastern GoM. We find a higher number of AEs using both satellite and model data in the western GoM (5,365 and 5,348) than the eastern GoM (4,593 and 3,581) during the period of study (Figure 8). The number of AEs found in the western GoM between satellite and model observations varied by only 17 eddies. Interestingly, in the eastern GoM, nearly 1,000 fewer AEs were identified using model output compared to satellite data. Spatial maps (Figures 5a and 5g) show that this is most likely due to the low number of coastal AEs identified in the model. The spatial distribution of CEs shows even more differences between satellite and model output. While the satellite data identified fewer CEs in the western GoM (5,395) than the eastern GoM (6,080), model output found more CEs in the western GoM (6,532) than the eastern GoM (4,495). This discrepancy is evident in the spatial maps (Figures 5m and 5s) where more CEs are

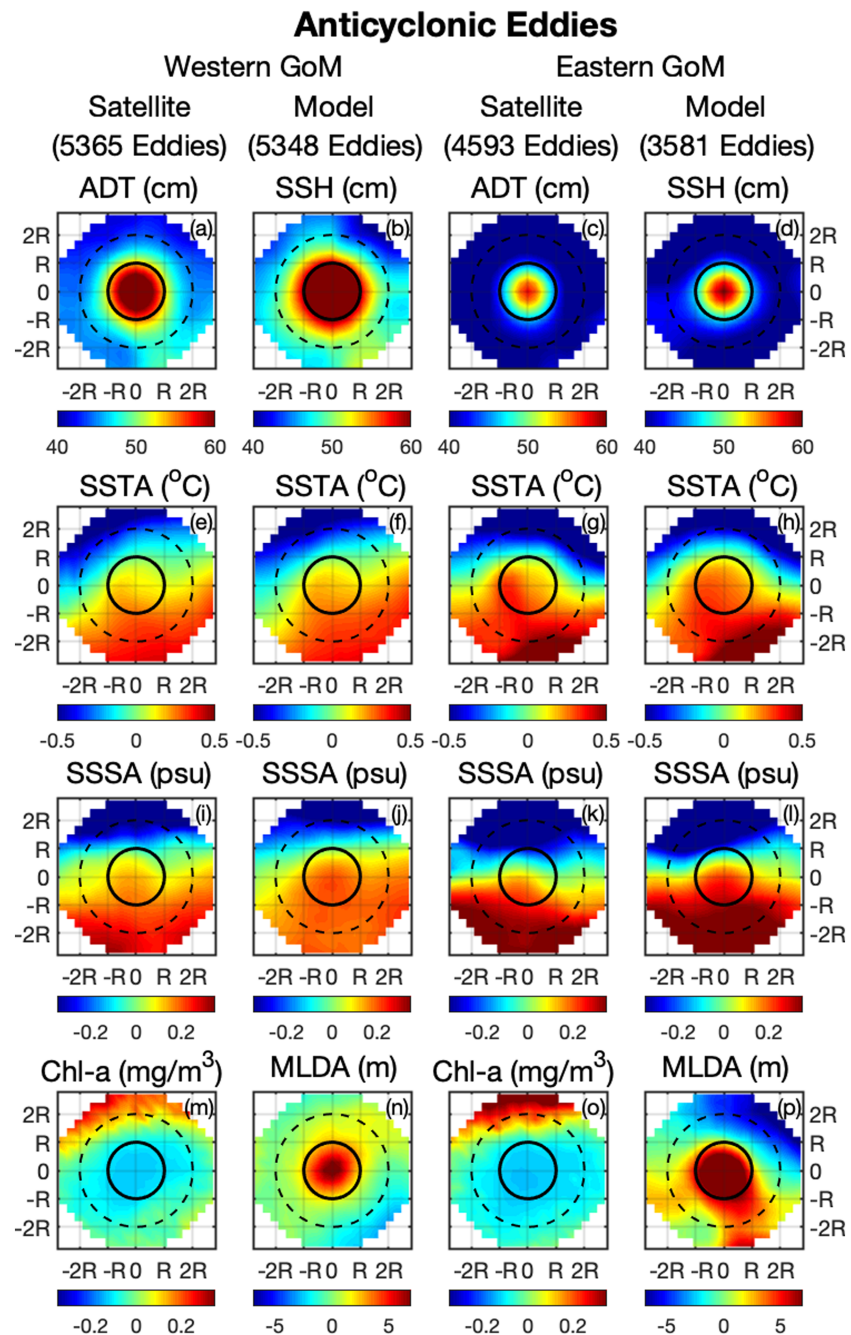


Figure 8. Composites of anticyclonic eddies in the western ($>90^{\circ}\text{W}$) and eastern ($<90^{\circ}\text{W}$ and $>21^{\circ}\text{N}$) GoM from satellite and model output. ADT, absolute dynamic topography; SSH, sea surface height; SSTA, sea surface temperature anomaly; SSSA, sea surface salinity anomaly; Chl-a, chlorophyll-a concentration (anomaly); MLDA, mixed layer depth anomaly.

identified in the LC region and the west Florida Shelf in the satellite data than the model output. For both AEs and CE, the total amount of eddies predicted by the model was closer to the amount observed using satellite data in the western GoM than in the eastern GoM. The differences in number of eddies located in the western GoM between the satellite data and model analysis were 17 AEs and 1,137 CE, whereas in the eastern GoM, the differences were 1,012 AEs and 1,585 CE. This could be due to the presence of stronger surface circulation features in the eastern GoM, where more mesoscale eddy generation occurs (Figures 4q–4t).

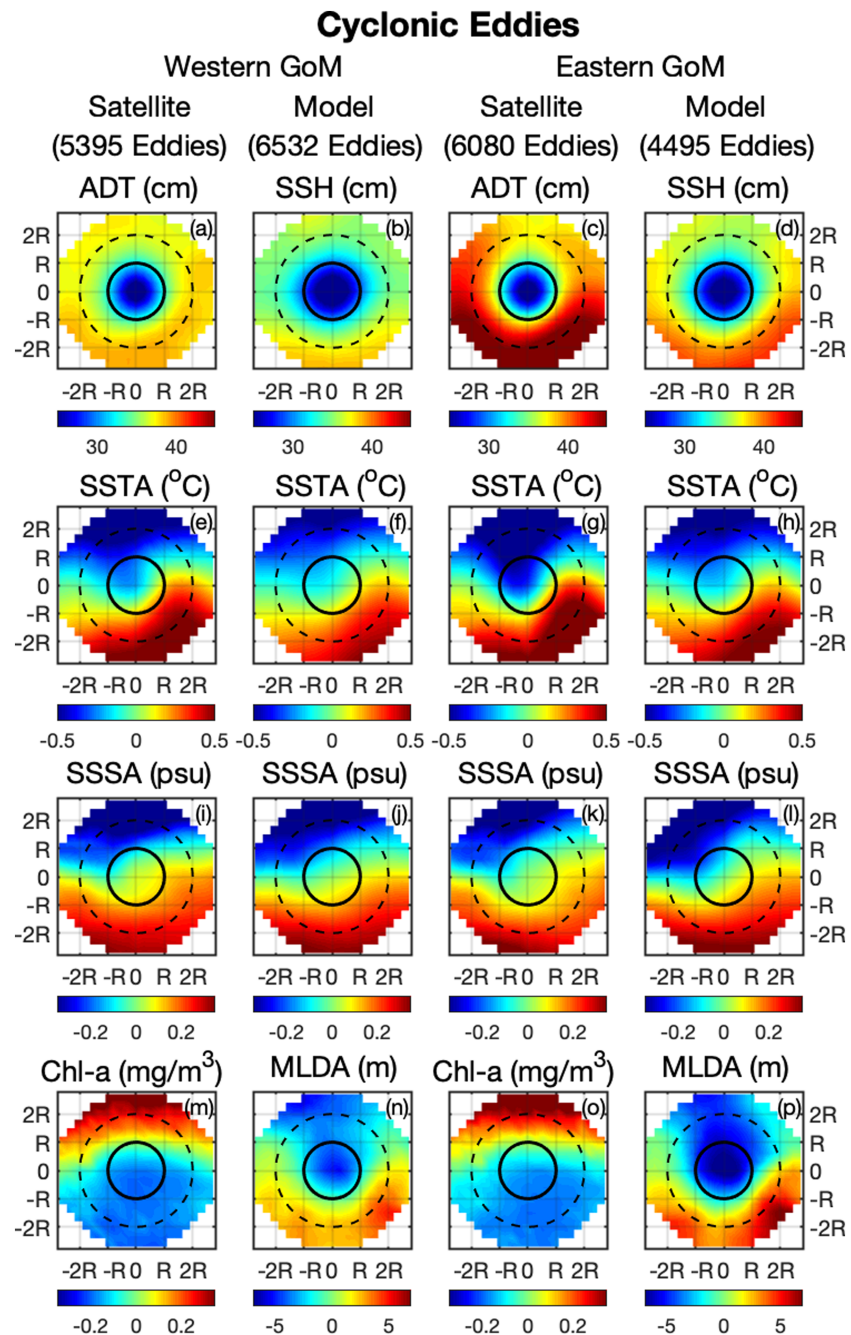


Figure 9. Same as Figure 8 but for cyclonic eddies.

This composite analysis of surface properties in which eddies are normalized by radius also allows for spatial comparison within and just outside of the eddy. In this analysis, we plot the properties from the center (0) out to three radii (3R), and we refer to areas within the normalized eddy to be within one radius (1R) and the area outside of one eddy radius to be outside 1R. Magnitudes of ADT and SSH are similar between the satellite and the model, although the model predicts a greater spatial extent (outside 1R) of the SSH maximum across AEs and CE in both subbasins (Figures 8a–8d and 9a–9d). In AEs, the gradient of ADT/SSH is much gentler in the western GoM than that in the eastern GoM, where extremely low values (<40 cm) dominate outside 1R. CEs show a similar pattern, as greater values of ADT/SSH (~45 cm) are found outside of the eddy in the eastern GoM, but much lower values (~35 cm) are present outside of the eddy in the western GoM. The ADT and SSH values were compared for spatial correlation, and correlation coefficients (r)

indicate high spatial correlation between the satellite and model data sets. The correlation coefficients of sea level for AEs (CEs) in the eastern and western GoM were 0.95 and 0.98 (0.96 and 0.95), respectively. This indicates strong spatial correlation in both subbasins but also shows higher spatial correlation with respect to sea level in the western GoM.

Both multiparameter composites reflect the large-scale gradients seen in the climatology, with low SSTA, low SSSA, and high Chl-a to the north. AEs and CEs differ in how these features are present within 1R, however. In the case of AEs, positive SSTAs (~ 0.4 °C) are present in the eastern GoM at the eddy core, while negative SSTAs (less than -0.3 °C) can be observed outside of 1R. In the western GoM, these negative SSTAs are mainly found to the northwest of the eddy center, whereas in the eastern GoM, they are found to wrap around the northern edge of the eddy. Additionally, the highest anomalies both inside and outside the eddy are found in the eastern GoM. This is likely representative of the climatological features in the eastern GoM including the LC. Since the LC brings anomalously warm water into the GoM from the Caribbean Sea, but coastal waters remain consistently cooler in the western and eastern sides of the basin (Figures 1b and 1f), there is a sharper gradient in temperature in the eastern GoM compared to the western GoM, where temperature is more homogenous. Therefore, it is likely that the surface signatures of SSTA within AEs are greatly impacted by the climatological features in the eastern GoM. In the western GoM, both the anomalies at the core of the eddy and surrounding the eddy are lower in magnitude (only ~ 0.25 °C at the center and approximately -0.25 °C outside the eddy edge). This could also indicate that as AEs follow the path of LCE propagation from the eastern side of the basin to the western side, their temperature characteristics at the surface are eroded by air-sea interaction over their lifetime.

When comparing SSTA in CEs, we find that both spatial distribution and magnitude of the anomalies are similar between eastern and western GoM (Figures 9e–9h). Negative SSTAs dominate the eddy center, while positive SSTAs are observed surrounding CEs across the western and eastern GoM. The cyclonic rotation of these eddies is evident in the positive SSTAs wrapping to the eastern side of the eddy, and the negative SSTAs wrapping around the western side. The difference, however, is between satellite and model observations. SSTAs inferred from satellite (model) data are found to have higher (lower) values at the core of approximately -0.45 °C (approximately -0.2 °C) and outside 1R of ~ 0.4 °C (~ 0.25 °C). There is a sharper gradient observed in satellite-derived SSTA in both the western and eastern GoM than model-derived SSTA. SSTA data between satellite and model data were also compared for spatial correlation. The correlation coefficients in regard to SSTA for AEs and CEs in the eastern and western GoM were all 0.99. This is the highest correlation coefficient observed between the satellite and model across all spatial features that were compared. This result indicates that HYCOM captures SST variability at the surface better than other features and may be due to the satellite data that are assimilated into the model.

Both AEs and CEs display negative SSSAs in their northern half and positive SSSAs in their southern half. A notable difference is that in AEs, the SSSA gradient is much sharper in the eastern GoM than the western GoM, with changes in SSSA greater than 0.4 within 1R, whereas a gentle SSSA gradient is found in the western GoM (Figures 8i–8l). Additionally, AEs in the western GoM were found to have positive SSSAs (~ 0.2 psu) throughout most of their core, wherein the eastern GoM AEs displayed cores with SSSAs of varying sign. There is not much difference in the spatial pattern or magnitude of the anomalies between eddies identified in the satellite and model output for AEs. CEs on average exhibited SSSAs of relatively small magnitudes throughout their core (~ 0 psu; Figures 9i–9l). Unlike AEs, where negative salinity anomalies are found all across the northern edge, CEs displayed negative SSSAs (approximately -0.25 psu) that were shifted to the northwest. This is most likely representative of the tendency for CEs to entrain low-salinity waters (shown in Figure 6) through eddy trapping. There is not much difference observed either between satellite and model observations or between sides of the basin. SSSAs were compared for spatial correlation, and correlation coefficients indicate high spatial correlation between the satellite data and model observations. The correlation coefficients for AEs (CEs) in the eastern and western GoM were found to be 0.97 and 0.98 (0.99 and 0.98), respectively. All correlation coefficients calculated for each variable (sea level, temperature, and salinity) indicate high positive spatial correlation between the data sets.

The spatial pattern of Chl-a concentration anomalies (Figures 8m and 8o and 9m and 9o) follows that of SSSA and SSTA, with higher magnitudes (~ 0.15 mg/m³ in AEs and ~ 0.25 mg/m³ in CEs) found along the northern edge of the eddies, which is representative of the high coastal productivity shown in Figure 1d.

AEs display both a smaller positive anomaly to the north and a smaller negative anomaly at their center (approximately -0.05 mg/m^3) than CEs (approximately -0.15 mg/m^3). The entrainment of highly productive waters to the eddy center as displayed in Figure 6d is not reflected in the composites. Unlike the composite analysis of Chl-a performed by Chelton, Gaube, et al. (2011), Gaube et al. (2014), and Dawson et al. (2018), we do not observe evidence of eddy stirring or eddy trapping of Chl-a in the eddy composites. This is likely due to the high variance in eddy interaction with waters having high concentrations of Chl-a, as we are mixing near-coastal and open-water eddies. Although eddy stirring is visible in the isolated instance shown in Figure 6, when averaged across all CEs, this mechanism does not dominate Chl-a concentration. This isolated eddy was relatively large and long lived, but most CEs within the GoM are of small radius and amplitude in coastal regions (Figure 4). These smaller CEs do not always interact with the highly biologically productive waters in the northern GoM over their short lifetimes and therefore do not have negative Chl-a anomalies at their core.

The local MLDAs found in AEs are of similar magnitude across the western and eastern GoM ($>5 \text{ m}$ at the eddy center; Figures 8n and 8p). However, the spatial distribution of MLDA outside 1R differs greatly between the two subbasins. Negative MLDAs (approximately -2 m) are found to the southeast in the western GoM, while MLDAs of larger magnitude (approximately -5 m) are found to the northeast in the eastern GoM. This is likely due to the shape of the basin, wherein the eastern GoM eddies are bounded by the west Florida Shelf to the northwest, but in the western GoM, eddies are bounded to the southwest by the Yucatan Shelf. In CEs, there is not much difference in the spatial distribution of MLDA across the western and eastern GoM. Both subbasins exhibited negative MLDAs at their center and to the north and positive MLDAs along their southern edge. However, the magnitude of these MLDAs vary across the subbasins, with negative (positive) anomalies reaching approximately -6 m ($\sim 5 \text{ m}$) in the eastern GoM but only reaching approximately -4 m ($\sim 3 \text{ m}$) in the western GoM. The mean MLD in the eastern GoM is higher (39 m) than the western GoM (31 m ; Figure 1h), and therefore, the percent change of the MLDA with respect to the mean MLD is significant and similar in both subbasins, with a 14% change in the eastern GoM and an 11% change in the western GoM. This pattern of larger magnitude anomalies in the eastern than western GoM is reflected across eddies of both rotation types. This is most likely due to the greater variation in MLD in the eastern GoM that responds to the LC intrusion than the western GoM where MLD is much more homogenous offshore (Figure 1h).

3.7. Eddy Vertical Structure

Figure 10 shows the mean characteristics (temperature and salinity) of the GoM across 25°N . This helps improve our understanding of the differing subsurface properties between eastern and western GoM that may affect those observed in eddies within these subbasins. In the western GoM, temperatures higher than 22°C persist from the surface down to $\sim 100 \text{ m}$, whereas in the eastern GoM, these temperatures are found from 0 to 150 m . Likewise, throughout the rest of the water column, waters of the same temperature are found approximately 50 m deeper in the eastern than the western GoM. This is likely due to the warm inflow of warm Caribbean Sea waters into the eastern GoM by the LC. Values of salinity between the two subbasins also vary at the surface and with depth. In the western GoM, surface values of $\sim 35.75 \text{ psu}$ persist across most longitudes from the surface to $\sim 20 \text{ m}$, except for a pocket of relatively fresh water found near the surface at 97°W likely due to riverine-sourced freshwater that has moved southward along the shelf. A subsurface salinity maximum of $\sim 36.45 \text{ psu}$ is found from ~ 100 to 120 m , whose saline waters reach down to $\sim 300 \text{ m}$. In the eastern GoM, however, surface salinities of $\sim 36 \text{ psu}$ make up the upper 20 m and are found across all longitudes from 80 – 90°W . The subsurface salinity maximum in this subbasin is of similar magnitude ($\sim 36.45 \text{ psu}$) but is found deeper in the water column from ~ 120 – 190 m . Salinities of $>35.75 \text{ psu}$ are found to depths of $\sim 370 \text{ m}$. This is consistent with Morrison et al. (1983), which described this subsurface high-salinity water as subtropical underwater also called Caribbean water. This Caribbean water is transported into the GoM by the LC at a rate of approximately 2.6 Sv (Lugo-Fernández et al., 2016) and spreads due to the advection by LCEs. The rest of the Gulf exhibits slightly lower salinities in the upper 250 m , which can be attributed to the formation of Gulf Common Water due to strong vertical mixing along the outer edge of the LC (Morrison et al., 1983).

The combination of greater temperature and salinity values that reach deeper into the water column in the eastern GoM depresses the isopycnals in this region, which is especially evident in the upper layers in which the $1,027\text{-kg/m}^3$ isopycnal reaches $\sim 20 \text{ m}$ further in the eastern than the western GoM, for example. With

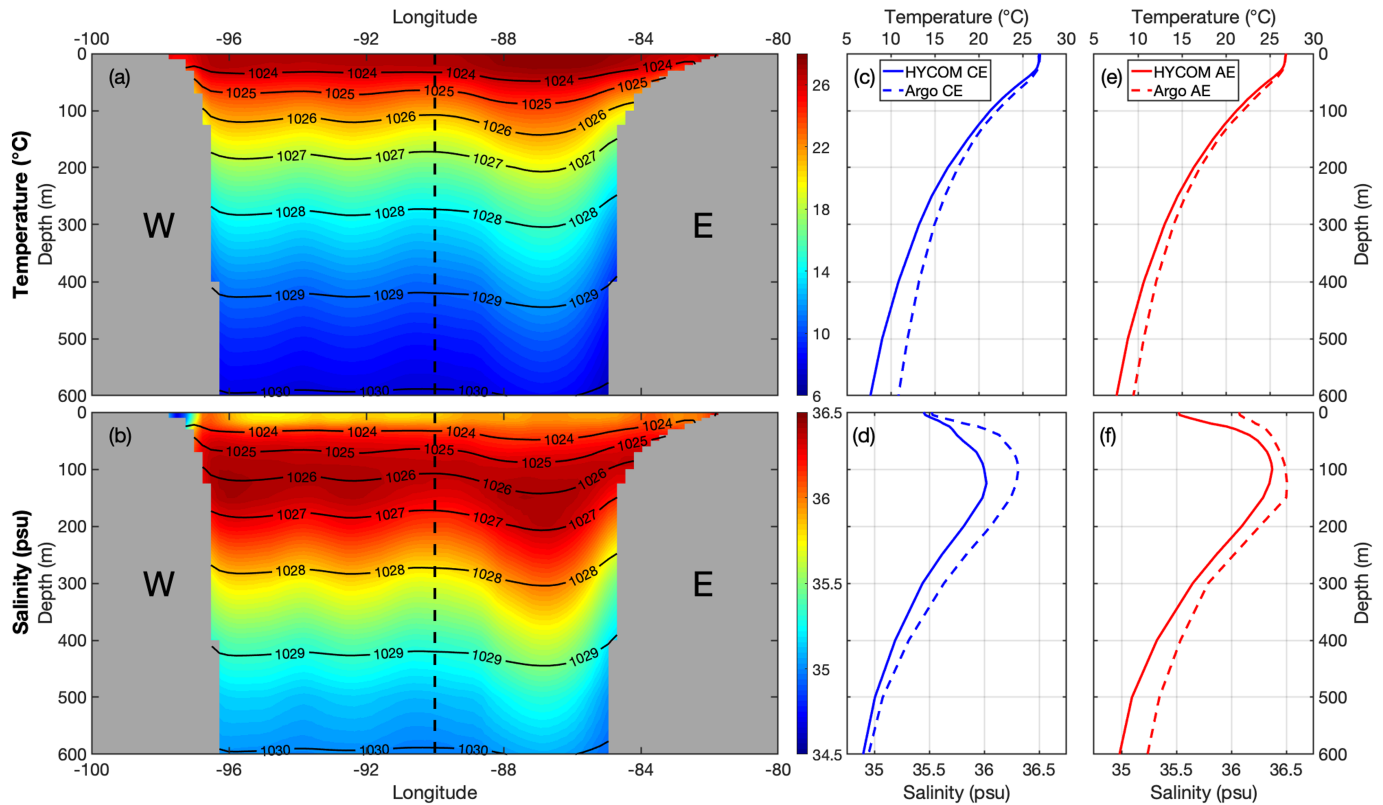


Figure 10. Mean zonal cross section of HYCOM (a) temperature and (b) salinity along 25°N from 2016–2018. Black contours indicate isopycnals every 1 kg/m³. Black dashed lines represent partition used in composite analysis of the eastern (<90°W and >21°N) and western (>90°W) GoM. Vertical mean profiles of temperature and salinity for (c) and (d) CEs and (e) and (f) AEs. Solid lines represent HYCOM data, while dashed lines represent Argo float data.

increasing depth, the difference in densities between the two water masses is less visible, in which the 1,029-kg/m³ isopycnal only exhibits ~10-m difference between eastern and western GoM. The varying characteristics of temperature, salinity, and density are due to differences in large-scale circulations between the two subbasins. The LC, which brings warm, saline waters into the eastern GoM, dominates circulation in this region. As the LC sheds LCEs that propagate westward, they carry this high-temperature and salinity signature with them into the western GoM (Elliot, 1982). It is likely that as these eddies decay, their density perturbations relax, resulting in upper-ocean upwelling in these AEs, degrading the warm, salty signature at the surface (McGillicuddy, 2016). Additionally, the deeper temperature and salinity signature in the eastern GoM compared to the western GoM is a result of the deepening of isohalines during formation in AEs, which occurs primarily in the eastern GoM.

In order to show the mean vertical structure exhibited by eddies within the GoM, and to further validate our use of HYCOM for eddy depth composite analysis, we plot the mean vertical temperature and salinity profiles of CEs and AEs using both HYCOM and Argo float data (Figures 10c–10f). First, we identify Argo floats that surface in either CEs and AEs during our time period identified from altimetry and calculate the average of these profiles. We then compare both these Argo profiles with both the mean temperature and salinity profiles within the modeled eddies. Both HYCOM and Argo show average temperatures within CEs and AEs of approximately 27 °C from the surface to 25-m depth. HYCOM accurately reflects the vertical temperature structure within these eddies, although HYCOM underestimates Argo temperature to a greater degree with increasing depth (Figures 10c and 10e). In salinity, HYCOM accurately reflects the vertical structure of these eddies, although the agreement between HYCOM and Argo is not as strong at the surface. The greatest disagreement between the products occurs at the subsurface salinity maximum in both CEs and AEs (~100 m; Figures 10d and 10f). HYCOM also underestimates Argo salinity in both CEs and AEs, but by a greater magnitude, and is more variable with depth than temperature. The tendency for HYCOM to underestimate both temperature and salinity is also shown in Figure 2, where we show that HYCOM has a

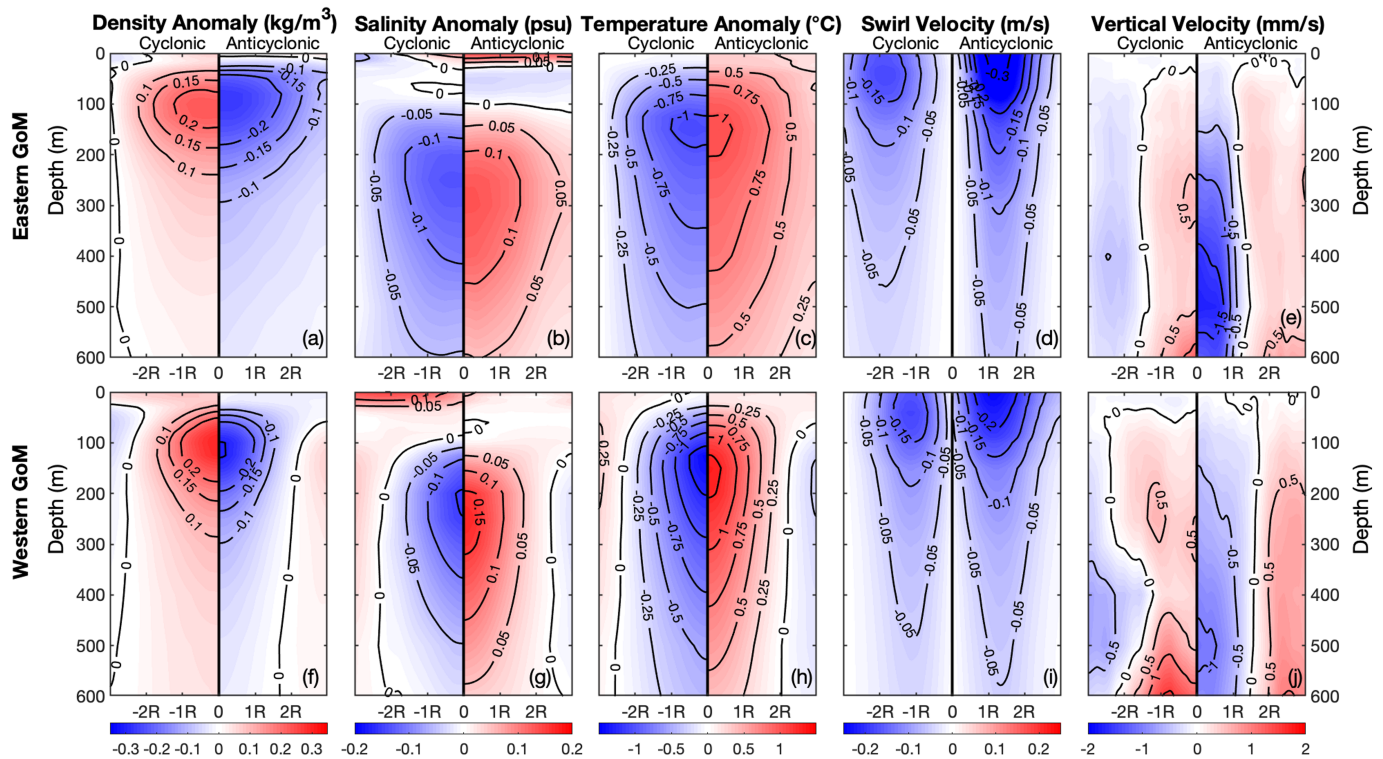


Figure 11. Zonal cross-section at the eddy center across composite cyclonic and anticyclonic eddies. (a, f) density anomaly (kilogram per cubic meter), (b, g) salinity anomaly (psu), (c, h) temperature anomaly ($^{\circ}\text{C}$), (d, i) swirl velocity (meridional component; meter per second), and (e, j) vertical velocity (millimeter per second) within three radii of the eddy center in the eastern (a–e; $<90^{\circ}\text{W}$ and $>21^{\circ}\text{N}$) and western (f–j; $>90^{\circ}\text{W}$) GoM. Cyclonic eddies are on the left and anticyclonic eddies are on the right within each subplot.

negative bias in both parameters. These profiles show that although HYCOM does underestimate these parameters, this model still correctly reproduces the observed eddy vertical structures (the shape of the vertical temperature and salinity distribution), and we are therefore confident in our use of HYCOM to depict the composite depth structures of eddies within the GoM.

In Figure 11, we analyze the vertical structure of CEs and AEs within the western and eastern GoM to investigate differences in the thermohaline structure of the eddies. Both CEs and AEs across the entire GoM seem to be subsurface-intensified, with maximum density anomalies at 80- to 120-m depth (Figures 10a and 10f). Density anomalies of CEs (AEs) are of smaller magnitude in the eastern GoM with values of 0.2 kg/m^3 (-0.25 kg/m^3) than the western GoM, with values of 0.3 kg/m^3 (-0.3 kg/m^3). The density anomalies in AEs reach deeper ($\sim 300 \text{ m}$) than CEs ($\sim 230 \text{ m}$) in the eastern GoM. This difference is not present in the western GoM, however, with both AEs and CEs reaching down to 300 m . A primary difference between eddies in the eastern and western GoM is the vertical position of their cores. For eddies of both rotation types, the maximum density, salinity, and temperature anomalies are found at shallower depths in the western GoM. For example, maximum salinity anomalies for composite CEs are found at $\sim 250 \text{ m}$ in the eastern GoM and at $\sim 210 \text{ m}$ in the western GoM. Likewise, maximum temperature anomalies for composite CEs occur at $\sim 170 \text{ m}$ in the eastern GoM and at $\sim 150 \text{ m}$ in the western GoM. This regional difference, also noted in Figure 10, is most likely the result of relatively saline waters from the LC and relatively fresh waters from river discharge in the northern GoM producing strong horizontal and vertical gradients, resulting in greater vertical stratification. In the western GoM, surface and subsurface properties are much more homogenous and therefore eddy cores are less affected by local stratification.

Overall, maximum salinity anomalies (Figures 11b and 11g) are found at greater depths ($\sim 250 \text{ m}$) than maximum temperature anomalies ($\sim 170 \text{ m}$; Figures 11c and 11h) in both the eastern and the western GoM. This is due to the large-scale vertical structure of these properties within the GoM, whose mean values are shown

in Figure 10 in which temperature maximums occur at the surface and persist for approximately 20 m until the thermocline, where temperature begins to decrease drastically. Salinity, however, exhibits lower values at the surface and reaches their maximum values and stronger gradients in the subsurface (Figure 10). Because of these varying large-scale temperature and salinity structures, the maximum temperature anomalies within eddies, mainly induced by the vertical displacements of the isopycnal layers (Figures 5e and 6e), are found to occur at a shallower depth than the maximum salinity anomalies.

The tendency for anomalies to be greater in magnitude as well as tighter in the western GoM than the eastern GoM is also visible in the salinity anomalies (Figures 11b and 11g) and temperature anomalies (Figures 11c and 11h). In the eastern GoM, the composite CE has a negative salinity anomaly core of approximately -0.15 psu, while the composite AE has a positive salinity anomaly core of ~ 0.15 psu (Figure 11b). Salinity anomalies observed for CEs in the eastern GoM show a vertical pattern of negative anomalies from 0–70 m, to positive from 70–100 m, then to negative again down to 600 m. However, the opposite is observed in AEs, where there are positive salinity anomalies at the surface to 40 m, a layer of negative anomalies from 40–110 m, then positive anomalies with depth to 600 m. This is due to the vertical displacement of the salinity structure that can be seen in Figure 10. Both CEs and AEs have differing vertical salinity profiles at their core, and since they interact with low-salinity water at the surface in different ways (CEs trap and AEs advect around the edge), the anomalies of salinity at the surface show positive in AEs and negative in CEs. CEs are formed from within the GoM, whereas the large anticyclonic LCEs are formed from Caribbean water that is saltier (Morrison et al., 1983). This difference in water masses from which these eddies are formed could also be the reason for variable salinity anomalies at their core and can be used to help distinguish an eddy of one rotation type from the other (Rudnick et al., 2015). In the western GoM, where there is no intrusion of saline waters via LC and less low-salinity water interaction as well, the salinity anomalies at the surface are relatively similar but with depth showing positive salinity anomalies of >0.15 psu in AEs and <-0.15 psu in CEs. This difference in salinity anomaly between western and eastern GoM is representative of the mean characteristics shown in Figures 1c and 1g and 10, where long-term salinity gradients that influence local stratification are much sharper in the eastern GoM than the western GoM.

Temperature anomalies show similar patterns to salinity and density when concerning magnitude with lower (higher) anomalies in the eastern (western) GoM (Figures 11c and 11h). In the eastern GoM, CEs (AEs) displayed temperature anomaly cores of approximately -1.1 °C (~ 1.1 °C), as opposed to the western GoM, where CEs (AEs) displayed temperature anomaly cores of approximately -1.3 °C (~ 1.3 °C). Similar to the density anomalies, AE temperature anomalies reached deeper than CE temperature anomalies in the eastern GoM, with 0.5 °C (-0.5 °C in CEs) isotherm reaching down to approximately 580-m depth in AEs but only to approximately 480-m depth in CEs. The difference in vertical reach of temperature anomalies is lesser in the western GoM, but AEs (CEs) still reach deeper (shallower) to depths of ~ 550 m (~ 530 m).

Plots of swirl velocity (Figures 11d and 11i) help display the vertical extent of eddy velocities observed at the surface in previous analysis. In AEs, the magnitude of southward flow ($>0R$) is found to be ~ 0.25 m/s in the eastern GoM and ~ 0.2 m/s in the western GoM. This pattern is shown as well in Rivas et al. (2008) in which maximum velocities of an LCE of ~ 0.3 m/s were observed at ~ 50 m. In CEs, the southward flow ($<0R$) is found to be less than that of AEs at ~ 0.15 m/s in both the eastern and western GoM. CEs across both subbasins show a velocity core below the surface from ~ 30 – 80 -m depth, whereas the velocity core is found near the surface in AEs. When comparing depth composites of eddies between the two subbasins, it is clear that the eastern GoM is home to AEs with greater swirl velocities, while the CEs exhibit swirl velocities of similar magnitude between the two subbasins. Maximum AE swirl velocity reaches 0.34 m/s in the eastern GoM, while it only reaches 0.26 m/s in the western GoM. Most AEs are formed in the LC region and propagate westward and as they decay along this path, their velocity structure deteriorates as total vorticity decreases (Hamilton, 1992). This helps explain both the lower magnitude and less coherent structure of velocity in western GoM AEs. Composite analysis of vertical velocities (Figures 11e and 11j) shows the mean upwelling (downwelling) signatures in CEs (AEs), with positive velocities indicating upward motion. Greater values of negative vertical velocities were observed in eastern AEs (approximately -0.18 mm/s or 15 m/day) than western AEs (approximately -0.11 mm/s or -9.5 m/day). These values are an order of magnitude lower than the ones depicted for the particular large eddies presented in Figures 5 and 6. However, the obtained vertical velocity values in our composite analysis are representative of those measured by Rivas et al. (2008), who found negative vertical velocities with magnitudes of 1 and 2 mm/s in anticyclonic LCEs. Conversely,

greater positive vertical velocities were observed in western CEs (~ 0.12 mm/s) than eastern CEs (~ 0.07 mm/s). This is reflective of the pattern in swirl velocities, which displayed stronger flow in eastern AEs.

4. Conclusions

Large-scale features in the GoM dominate the spatial variability observed in the local eddy field. Features such as the LC, which brings warm, saline water into the GoM from the Caribbean Sea, and riverine outflow that delivers fresh, nutrient-rich water to the coastal northern GoM create a basin full of varying properties. The vertical structures of the mean salinity and temperature vary greatly between the eastern and western GoM due to the influence of the LC and eddy interaction with seasonal freshwater input. The saline waters sourced from the LC dominate the subsurface while seasonally present freshwater dominates the surface in the eastern GoM. Comparatively, the western GoM is much more homogenous in both salinity and temperature.

We found that in episodes of high numbers of basin-wide CEs, the number of AEs decreases, which typically occur immediately following the shedding of a large LCE. This is most likely due to the cyclonic LCFEs that congregate around the tip of the LC and force this shedding. Conversely, in periods where AEs dominate the GoM, there are not many CEs, which usually occur when the LC is extending. Occasionally, there are times in which the number of both AEs and CEs is high, when there is not one large rotation (cyclonic or anticyclonic) that dominates the flow in the basin. These spells are then balanced by a decrease in amplitude and radius of both types of eddy. This balance occurs because the region is spatially limited and is reflective of the shape of the GoM as a semienclosed basin, with only two main entry and exit points in the Yucatan Strait and the Florida Strait. A spatial analysis of eddy characteristics demonstrated that both AEs and CEs decrease in amplitude and radius, as well as temperature and salinity anomalies at the surface. Since the LC region in the southeastern GoM is a location of high eddy generation of both types, and climatological features show that the GoM is heavily influenced by air-sea interactions, it is most likely that due to these air-sea interactions, the surface characteristics of these eddies are eroded throughout their lifetime as they propagate westward. When comparing the satellite observations to model output, the model correctly displays spatial patterns of every characteristic measured. However, the model tends to underestimate some characteristics (amplitude, radius, and SSTA) and overestimate others (Rossby number and SSSA).

By isolating one eddy of each type, we were able to more closely observe the processes by which the eddies interact with surrounding waters that help determine their surface characteristics. By isolating a CE, we found that the horizontal advection of low-salinity water in the northern GoM may create a negative salinity anomaly at its center. However, the upwelling associated with such a CE injects high-salinity subsurface waters into the surface, which can quickly erode the fresh signature. In the isolated AE, which we identified as a previously shed LCE, we observe that advection of low-salinity water along the eddy's eastern edge effectively surrounds the eddy in anomalously fresh water, which can create a positive salinity anomaly at its center. The deepening of isopycnals reveals the deep vertical structure of this LCE.

We analyzed the eastern and western sides of the GoM to help understand the effect differing climatological features may have on the eddy properties. In the eastern GoM, steep salinity gradients are observed in eddies of both circulation type, while in the western GoM, the observed salinity gradients are much gentler. This is likely a reflection of the greatly varying surface salinities in the eastern GoM (saline waters from the LC and fresh waters from major river discharge), wherein the western GoM is comparatively homogenous. Originally, the positive SSTAs in AEs and negative SSTAs in CEs were thought to reflect downwelling and upwelling mechanisms present in each eddy. However, through composite analysis of the depth structures of these eddies, along with the tendency for air-sea interaction to play a part in the determination of surface eddy properties, we conclude that temperature anomalies at the surface are not useful in identifying AEs from CEs. Eddies of both circulation types appear to be surface intensified in terms of vorticity, as the swirl velocities reach maximum values at the surface. The eddies exhibit maximum temperature, salinity, and therefore density anomalies below the surface due to vertical motions and the displacements of water masses.

The purpose of this study was to expand the knowledge of the entire GoM mesoscale eddy field both in the surface and in the subsurface. Our objectives were to investigate spatial distribution of eddy properties in both rotation types and to explore the effect of long-term climatological features on eddy properties. We

first described the dominant features of the basin such as warm, saline LC waters and cool, fresh coastal waters that may have an effect on the properties of individual eddies that inhabit the GoM. We showed that these climatological features heavily affect both the surface and subsurface eddy properties. Sharper horizontal temperature and salinity gradients in the eastern GoM create steep gradients within the eddy centers, wherein the more homogenous western GoM waters and horizontal gradients of temperature and salinity are much gentler overall and within the eddies. Composite analysis of eddy vertical structure revealed stronger flow in the eastern than western GoM, which also have density anomalies deeper in the water column. These eastern eddies are typically younger, whereas western GoM eddies have begun to decay as their properties can be eroded by air-sea interaction. The dominance of climatological surface characteristics overshadowed any vertical movements of water within the eddy. Through spatial, composite, and depth analysis, we achieved our objectives and successfully describe surface and subsurface properties of the entire mesoscale eddy field within the GoM. Future works could include the comparison of multiple models along with additional in situ data in order to fully investigate the vertical eddy structure and extension of the time period to include previous satellite measurements of temperature and salinity as well as a longer in situ record.

Acknowledgments

ADT are provided by the Copernicus Marine Environmental Monitoring Service (CMEMS; marine.copernicus.eu). SMAP SSS data are available via NASA's Jet Propulsion Laboratory Physical Oceanography Distributed Active Archive Center (PO.DAAC), which are freely available to anyone with NASA Earthdata login credentials (https://podaac-tools.jpl.nasa.gov/drive/files/SalinityDensity/smap/L3/JPL/V4.2/8day_running; DOI: 10.5067/SMP42-3TMCS). SST used in this research is available from NOAA National Climatic Data Center (NCDC; ncdc.noaa.gov/oisst; DOI:10.1175/2007JCLI1824.1). GlobColour data (<http://globcolour.info>) used in this study have been developed, validated, and distributed by ACRI-ST, France. Argo profile data are made available by the Naval Research Laboratory GODAE (nrlgodae1.nrlmry.navy.mil/argo/argo.html) and also we would like to acknowledge Argo project <http://doi.org/10.17882/42182>. Lastly, regional HYCOM model simulations are available at <https://www.hycom.org/data/goml0pt04/expt-32pt5>. The authors would like to thank the anonymous reviewers and editor whose comments significantly contributed to the improvement of this paper.

References

- Aguéiou, H., Dadou, L., Chaigneau, A., Morel, Y., & Alory, G. (2019). Eddies in the tropical Atlantic Ocean and their seasonal variability. *Geophysical Research Letters*, *46*, 12,156–12,164. <https://doi.org/10.1029/2019GL083925>
- Alvera-Azcárate, A., Barth, A., & Weisberg, R. H. (2008). The surface circulation of the Caribbean Sea and the Gulf of Mexico as inferred from satellite altimetry. *Journal of Physical Oceanography*, *39*, 640–657. <https://doi.org/10.1175/2008JPO3765.1>
- Bleck, R. (2002). An oceanic general circulation model framed in hybrid isopycnic-Cartesian coordinates. *Ocean Modelling*, *4*(1), 55–88. [https://doi.org/10.1016/S1463-5003\(01\)00012-9](https://doi.org/10.1016/S1463-5003(01)00012-9)
- Bleck, R., & Boudra, D. (1981). Initial testing of a numerical ocean circulation model using a hybrid (quasi-isopycnic) vertical coordinate. *Journal of Physical Oceanography*, *11*, 755–770. [https://doi.org/10.1175/1520-0485\(1981\)011<0755:ITOANO>2.0.CO;2](https://doi.org/10.1175/1520-0485(1981)011<0755:ITOANO>2.0.CO;2)
- Bratkovich, A., Dinnel, S. P., & Goolsby, D. A. (1994). Variability and prediction of freshwater and nitrate fluxes for the Louisiana-Texas Shelf: Mississippi and Atchafalaya River source functions. *Estuarine Research Federation*, *17*, 766–778. <https://doi.org/10.2307/1352746>
- Brokaw, R. J., Subrahmanyam, B., & Morey, S. L. (2019). Loop Current and eddy-driven salinity variability in the Gulf of Mexico. *Geophysical Research Letters*, *46*, 5978–5986. <https://doi.org/10.1029/2019GL082931>
- Chaigneau, A., Gizolme, A., & Grados, C. (2008). Mesoscale eddies off Peru in altimeter records: Identification algorithms and eddy spatio-temporal patterns. *Progress in Oceanography*, *79*(2-4), 106–119. <https://doi.org/10.1016/j.pocean.2008.10.013>
- Chaigneau, A., Le Texier, M., Eldin, G., Grados, C., & Pizarro, O. (2011). Vertical structure of mesoscale eddies in the eastern South Pacific Ocean: A composite analysis from altimetry and Argo profiling floats. *Journal of Geophysical Research*, *116*, C11025. <https://doi.org/10.1029/2011JC007134>
- Chang, Y. L., & Oey, L. Y. (2010). Eddy and wind-forced heat transports in the Gulf of Mexico. *Journal of Physical Oceanography*, *40*, 2481–2495. <https://doi.org/10.1175/2010JPO4460.1>
- Chassignet, E. P., Smith, L. T., Halliwell, G. R., & Bleck, R. (2003). North Atlantic simulations with the Hybrid Coordinate Ocean Model (HYCOM): Impact of the vertical coordinate choice, reference pressure, and thermobaricity. *Journal of Physical Oceanography*, *33*(12), 2504–2526. [https://doi.org/10.1175/1520-0485\(2003\)033<2504:NASWTH>2.0.CO;2](https://doi.org/10.1175/1520-0485(2003)033<2504:NASWTH>2.0.CO;2)
- Chelton, D. B., Gaube, P., Schlax, M. G., Early, J. J., & Samelson, R. M. (2011). The influence of nonlinear eddies on near-surface oceanic chlorophyll. *Science*, *334*, 328–332. <https://doi.org/10.1126/science.1208897>
- Chelton, D. B., Schlax, M. G., & Samelson, R. M. (2011). Global observations of nonlinear mesoscale eddies. *Progress in Oceanography*, *91*(2), 167–216. <https://doi.org/10.1016/j.pocean.2011.01.002>
- Cochrane, J. D. (1972). Separation of an anticyclone and subsequent developments in the Loop Current (1969), Contribution on the Phys. Oceanography of the Gulf of Mexico: 91-106
- Cummings, J. A. (2005). Operational multivariate ocean data assimilation. *Quarterly Journal of the Royal Meteorological Society*, *131*(613), 3583–3604. <https://doi.org/10.1256/qj.05.105>
- Dawson, H. R. S., Strutton, P. G., & Gaube, P. (2018). The unusual surface chlorophyll signatures of Southern Ocean eddies. *Journal of Geophysical Research: Oceans*, *123*, 6053–6069. <https://doi.org/10.1029/2017JC013628>
- Donohue, K. A., Watts, D. R., Hamilton, P., Leben, R., & Kennelly, M. (2016). Loop current eddy formation and baroclinic instability. *Dynamics of Atmospheres and Oceans*, *76*, 195–216. <https://doi.org/10.1016/j.dnatmoce.2016.01.004>
- Donohue, K. A., Watts, D. R., Hamilton, P., Leben, R., Kennelly, M., & Lugo-Fernández, A. (2016). Gulf of Mexico loop current path variability. *Dynamics of Atmospheres and Oceans*, *76*, 174–194. <https://doi.org/10.1016/j.dnatmoce.2015.12.003>
- Douglass, E. M., & Richman, J. G. (2015). Analysis of ageostrophy in strong surface eddies in the Atlantic Ocean. *Journal of Geophysical Research: Oceans*, *120*, 1490–1507. <https://doi.org/10.1002/2014JC010350>
- Ducet, N., Le Traon, P. Y., & Reverdin, G. (2000). Global high-resolution mapping of ocean circulation from TOPEX/Poseidon and ERS-1 and-2. *Journal of Geophysical Research*, *105*(C8), 19,477–19,498. <https://doi.org/10.1029/2000JC900063>
- Elliot, B. A. (1982). Anticyclonic rings in the Gulf of Mexico, *J. Physical Oceanography*, *12*, 1292–1309. [https://doi.org/10.1175/1520-0485\(1982\)012<1292:ARITGO>2.0.CO;2](https://doi.org/10.1175/1520-0485(1982)012<1292:ARITGO>2.0.CO;2)
- Fournier, S., Reager, J. T., Lee, T., Vazquez-Cuervo, J., David, C. H., & Gierach, M. M. (2016). SMAP observes flooding from land to sea: The Texas event of 2015. *Geophysical Research Letters*, *43*, 10–338. <https://doi.org/10.1002/2016GL070821>
- Fratantoni, P. S., Lee, T. N., Podestá, G. P., & Muller-Karger, F. (1998). The influence of Loop Current perturbations on the formation and evolution of Tortugas eddies in the southern Straits of Florida. *Journal of Geophysical Research*, *103*(C11), 24,759–24,779. <https://doi.org/10.1029/98JC02147>
- Gaube, P., McGillicuddy, D. J. Jr., Chelton, D. B., Behrenfeld, M. J., & Strutton, P. G. (2014). Regional variations in the influence of mesoscale eddies on near-surface chlorophyll. *Journal of Geophysical Research: Oceans*, *119*, 8195–8220. <https://doi.org/10.1002/2014JC010111>

- Gierach, M., & Subrahmanyam, B. (2007). Satellite data analysis of the upper ocean response to Hurricanes Katrina and Rita (2005) in the Gulf of Mexico. *IEEE Geoscience and Remote Sensing Letters*, 4(1), 132–136. <https://doi.org/10.1109/LGRS.2006.887145>
- Hall, C., & Leben, R. (2016). Observational evidence of seasonality in the timing of loop current eddy separation. *Dynamics of Atmospheres and Oceans*, 76, 240–267. <https://doi.org/10.1016/j.dynatmoce.2016.06.002>
- Hamilton, P. (1992). Lower continental slope cyclonic eddies in the central Gulf of Mexico. *Journal of Geophysical Research*, 97, 2185–2200. <https://doi.org/10.1029/91JC01496>
- Hamilton, P., Fargion, G. S., & Biggs, D. C. (1999). Loop current eddy paths in the Western Gulf of Mexico. *Journal of Physical Oceanography*, 29, 1180–1207. [https://doi.org/10.1175/1520-0485\(1999\)029<1180:LCEPIT>2.0.CO;2](https://doi.org/10.1175/1520-0485(1999)029<1180:LCEPIT>2.0.CO;2)
- Hamilton, P., Lugo-Fernández, A., & Sheinbaum, J. (2016). A Loop Current experiment: Field and remote measurements. *Dynamics of Atmospheres and Oceans*, 76, 156–173. <https://doi.org/10.1016/j.dynatmoce.2016.01.005>
- Hausmann, U., McGillicuddy, D. J. Jr., & Marshall, J. (2017). Observed mesoscale eddy signatures in Southern Ocean surface mixed-layer depth. *Journal of Geophysical Research: Oceans*, 122, 617–635. <https://doi.org/10.1002/2016JC012225>
- Huang, J., Xu, F., Zhou, K., Xiu, P., & Lin, Y. (2017). Temporal evolution of near-surface chlorophyll over cyclonic eddy lifecycles in the southeastern Pacific. *Journal of Geophysical Research: Oceans*, 122, 6165–6179. <https://doi.org/10.1002/2017JC012915>
- Le Traon, P. Y., Nadal, F., & Ducet, N. (1998). An improved mapping method of multisatellite altimeter data. *Journal of Atmospheric and Oceanic Technology*, 15, 522–534.
- Leben, R. R., & Born, G. H. (1993). Tracking Loop Current eddies with satellite altimetry. *Advances in Space Research*, 13(11), 325–333. [https://doi.org/10.1016/0273-1177\(93\)90235-4](https://doi.org/10.1016/0273-1177(93)90235-4)
- Lewis, J. K., Kirwan, A. D. Jr., & Forristall, G. Z. (1989). Evolution of a warm-core ring in the Gulf of Mexico: Lagrangian Observations. *Journal of Geophysical Research*, 94(C6), 8163–8178.
- Luecke, C. A., Arbic, B. K., Bassette, S. L., Richman, J. G., Shriver, J. F., Alford, M. H., et al. (2017). The global mesoscale eddy available potential energy field in models and observations. *Journal of Geophysical Research: Oceans*, 122, 9126–9143. <https://doi.org/10.1002/2017JC013136>
- Lugo-Fernández, A., Leben, R., & Hall, C. (2016). Kinematic metrics of the Loop Current in the Gulf of Mexico from satellite altimetry. *Dynamics of Atmospheres and Oceans*, 76, 268–282. <https://doi.org/10.1016/j.dynatmoce.2016.01.002>
- Maritorena, S., & Siegel, D. A. (2005). Consistent merging of satellite ocean color data sets using a bio-optical model. *Remote Sensing of Environment*, 94(4), 429–440. <https://doi.org/10.1016/j.rse.2004.08.014>
- Maul, G. A., & Vukovich, F. M. (1993). The relationship between variations in the Gulf of Mexico Loop Current and Straits of Florida volume transport. *Journal of Physical Oceanography*, 23, 785–796. [https://doi.org/10.1175/1520-0485\(1993\)023<0785:TRBVIT>2.0.CO;2](https://doi.org/10.1175/1520-0485(1993)023<0785:TRBVIT>2.0.CO;2)
- McGillicuddy, D. J. (2016). Mechanisms of physical-biological-biochemical interaction at the oceanic mesoscale. *Annual Review of Marine Science*, 8, 125–159. <https://doi.org/10.1146/annurev-marine-010814-015606>
- McGillicuddy, D. J., Anderson, L. A., Bates, N. R., Bibby, T., Buesseler, K. O., & Carlson, A. A. (2007). Eddy/wind interactions stimulate extraordinary mid-ocean plankton blooms. *Science*, 316(5827), 1021–1026. <https://doi.org/10.1126/science.1136256>
- Morey, S. L., Martin, P. J., O'Brien, J. J., Wallcraft, A. A., & Zavala-Hidalgo, J. (2003). Export pathways for river discharged fresh water in the northern Gulf of Mexico. *Journal of Geophysical Research*, 108(C10), 3303. <https://doi.org/10.1029/2002JC001674>
- Morey, S. L., Schroeder, W. W., O'Brien, J. J., & Zavala-Hidalgo, J. (2003). The annual cycle of riverine influence in the eastern Gulf of Mexico Basin. *Geophysical Research Letters*, 30(16), 1867. <https://doi.org/10.1029/2003GL017348>
- Morrison, J., Merrell, W., Key, R., & Key, T. (1983). Property distributions and deep chemical measurements within the western Gulf of Mexico. *Journal of Geophysical Research*, 88(C4), 2601–2608. <https://doi.org/10.1029/JC088iC04p02601>
- Otis, D. B., Le Hénaff, M., Kourafalou, V. H., McEachron, L., & Muller-Karger, F. E. (2019). Mississippi River and Campeche Bank (Gulf of Mexico) episodes of cross-shelf export of coastal waters observed with satellites. *Remote Sensing*, 11(6), 723. <https://doi.org/10.3390/rs11060723>
- Paluszkiwicz, T., Atkinson, L. P., Posmentier, E. S., & McClain, C. R. (1983). Observations of a Loop Current frontal eddy intrusion onto the West Florida Shelf. *Journal of Geophysical Research*, 88(C14), 9639–9651. <https://doi.org/10.1029/JC088iC14p09639>
- Pegliasco, C., Chaigneau, A., & Morrow, R. (2015). Main eddy vertical structures observed in the four major eastern boundary upwelling systems. *Journal of Geophysical Research: Oceans*, 120, 6008–6033. <https://doi.org/10.1002/2015JC010950>
- Pérez-Brunius, P., Furey, H., Bower, A., Hamilton, P., Candela, J., García-Carrillo, P., & Leben, R. (2018). Dominant circulation patterns of the deep Gulf of Mexico. *Journal of Physical Oceanography*, 48, 511–529. <https://doi.org/10.1175/JPO-D-17-0140.1>
- Reynolds, R. W., Smith, T. M., Liu, C., Chelton, D. B., Casey, K. S., & Schlax, M. G. (2007). Daily high-resolution-blended analyses for sea surface temperature. *Journal of Climate*, 20(22), 5473–5496. <https://doi.org/10.1175/2007JCLI1824.1>
- Rivas, D., Badan, A., Sheinbaum, J., Ochoa, J., & Cabdela, J. (2008). Vertical velocity and vertical heat flux observed within Loop Current eddies in the Central Gulf of Mexico. *Journal of Physical Oceanography*, 38, 2461–2481. <https://doi.org/10.1175/2008JPO3755.1>
- Rosburg, K., Donohue, K., & Chassignet, E. (2016). Three-dimensional model-observation comparison in the Loop Current region. *Dynamics of Atmospheres and Oceans*, 76, 283–305. <https://doi.org/10.1016/j.dynatmoce.2016.05.001>
- Rudnick, D., Gopalakrishnan, G., & Cornuelle, B. (2015). Cyclonic eddies in the Gulf of Mexico: Observations by underwater gliders and simulations by numerical model. *Journal of Physical Oceanography*, 45, 313–326. <https://doi.org/10.1175/JPO-D-14-0138.1>
- Sheinbaum, J., Athié, G., Candela, J., Ochoa, J., & Romero-Arteaga, A. (2016). Structure and variability of the Yucatan and Loop Currents along the slope and shelf break of the Yucatan Channel and Campeche Bank. *Dynamics of Atmospheres and Oceans*, 76, 217–239. <https://doi.org/10.1016/j.dynatmoce.2016.08.001>
- Souza, J. M. A. C., de Boyer Montégut, C., & Le Traon, P. Y. (2011). Comparison between three implementations of automatic identification algorithms for the quantification and characterization of mesoscale eddies in the South Atlantic Ocean. *Ocean Science*, 7(3), 317–334. <https://doi.org/10.5194/os-7-317-2011>
- Sturges, W., & Evans, J. C. (1983). On the variability of the Loop Current in the Gulf of Mexico. *Journal of Marine Research*, 41, 639–653. <https://doi.org/10.1357/002224083788520487>
- Sturges, W., Evans, J. C., Welsh, S., & Holland, W. (1992). Separation of warm-core rings in the Gulf of Mexico. *Journal of Physical Oceanography*, 23, 250–268. [https://doi.org/10.1175/1520-0485\(1993\)023<0250:SOWCRI>2.0.CO;2](https://doi.org/10.1175/1520-0485(1993)023<0250:SOWCRI>2.0.CO;2)
- Sturges, W., & Leben, R. (2000). Frequency of ring separations from the Loop Current in the Gulf of Mexico: A revised estimate. *Journal of Physical Oceanography*, 30, 1814–1819. [https://doi.org/10.1175/1520-0485\(2000\)030<1814:FORSFT>2.0.CO;2](https://doi.org/10.1175/1520-0485(2000)030<1814:FORSFT>2.0.CO;2)
- Sun, W., Dong, C., Tan, W., Liu, Y., He, Y., & Wang, J. (2018). Vertical structure anomalies of oceanic eddies and eddy-induced transports in the South China Sea. *Remote Sensing*, 10(795). <https://doi.org/10.3390/rs10050795>
- Trott, C. B., Subrahmanyam, B., Chaigneau, A., & Delcroix, T. (2018). Eddy tracking in the northwestern Indian Ocean during southwest monsoon regimes. *Geophysical Research Letters*, 45, 6594–6603. <https://doi.org/10.1029/2018GL078381>

- Trott, C. B., Subrahmanyam, B., Chaigneau, A., & Roman-Stork, H. L. (2019). Eddy-induced temperature and salinity variability in the Arabian Sea. *Geophysical Research Letters*, *46*, 2734–2742. <https://doi.org/10.1029/2018GL081605>
- Vazquez de la Cerda, A., Reid, R., Dimarco, S., & Jochens, A. (2005). Bay of Campeche circulation: An update. In W. Sturges, & A. Lugo-Fernandez (Eds.), *Circulation of the Gulf of Mexico: Observations and models, Geophysical Monograph Series*, (Vol. 161, pp. 279–293). Washington, DC: AGU.
- Vazquez-Cuervo, J., Fournier, S., Dzwonkowski, B., & Reager, J. (2018). Intercomparison of in-situ and remote sensing salinity products in the Gulf of Mexico, a river-influenced system. *Remote Sensing*, *10*(10), 1590.
- Vukovich, F. M. (1986). Aspects of the behavior of cold perturbations in the eastern Gulf of Mexico: A case study. *Journal of Physical Oceanography*, *16*(1), 175–188. <https://doi.org/10.1029/JC091iC02p02645>
- Walker, N., Pilley, C., Raghunathan, V., D'Sa, E., Leben, R., Hoffmann, N., et al. (2011). Impacts of loop current frontal cyclonic eddies and wind forcing on the 2010 Gulf of Mexico Oil spill. In *Monitoring and modeling the Deepwater Horizon oil spill: A record-breaking enterprise*, Geophysical Monograph Series (Vol. 195, pp. 103–116). Washington, DC: American Geophysical Union. <https://doi.org/10.1029/2011GM00120>
- Walker, N.D., R. Leben, S. Anderson, J. Feeney, P. Coholan, and N. Sharma, (2009), Loop Current frontal eddies based on satellite remote sensing and drifter data. OCS Study MMS 2009-023, US. Dep. Inter. Miner. Manag. Serv., Gulf Mex. OCS Reg., New Orleans, LA
- Weissman, D.E., S. Morey, & M. Bourassa, (2017), Studies of the effects of rain on the performance of the SMAP radiometer surface salinity estimates and applications to remote sensing of river plumes, In 2017 IEEE International Geoscience and Remote Sensing Symposium (IGARSS) (pp. 1491–1494).
- Yi, J., Du, Y., He, Z., & Zhou, C. (2014). Enhancing the accuracy of automatic eddy detection and the capability of recognizing the multi-core structures from maps of sea level anomaly. *Ocean Science*, *10*(1), 39. <https://doi.org/10.5194/os-10-39-2014>
- Zavala-Hidalgo, J., Morey, S. L., & O'Brien, J. J. (2003). Cyclonic eddies northeast of the Campeche Banks from altimetry data. *Journal of Physical Oceanography*, *33*, 623–629. [https://doi.org/10.1175/1520-0485\(2003\)033<0623:CENOTC>2.0.CO;2](https://doi.org/10.1175/1520-0485(2003)033<0623:CENOTC>2.0.CO;2)